Non-Linear & Adaptive Flight Control

August 2020

Mauro Villanueva Aguado

TUDelft

AE4-311
Non-Linear & Adaptive Flight Control

Take Home Assignment 1

Fault Tolerant Flight Control Using Model and Sensor based Nonlinear Dynamic Inversion

Mauro Villanueva Aguado - 4557824

Control & Simulation Department
Faculty of Aerospace Engineering
TU Delft, The Netherlands

Front Page Image © Maarten Visser [1]

Assignment Duration:	June 2020 – September 2020	
Supervisors:	Dr. ir. C.C. de Visser	Responsible Instructor
	Dr. ir. E. van Kampen	Assistant Professor

[1] https://www.flickr.com/photos/44939325@N02/13720867964/in/photostream/ [cited 30 March 2020]

List of Symbols

Symbol	Description	Unit
I	Mass Moment of Inertia	$[kg \cdot m^2]$
V	Velocity	$[m/s]$
m	Mass of Aircraft	$[kg]$
ρ	Air Density	$[kg/m^3]$
α	Angle of Attack	$[Rad]$
θ	Pitch Angle	$[Rad]$
ϕ	Roll Angle	$[Rad]$
β	Sideslip Angle	$[Rad]$
p	Roll Rate	$[Rad/s]$
q	Pitch Rate	$[Rad/s]$
r	Yaw Rate	$[Rad/s]$
X	Force in X_b axis in Body-Fixed Reference Frame	$[N]$
Y	Force in Y_b axis in Body-Fixed Reference Frame	$[N]$
Z	Force in Z_b axis in Body-Fixed Reference Frame	$[N]$
L	Moment in X_b axis	$[N \cdot m]$
M	Moment in Y_b axis	$[N \cdot m]$
N	Moment in Z_b axis	$[N \cdot m]$
A_X	Acceleration in X_b axis	$[m/s^2]$
A_Y	Acceleration in Y_b axis	$[m/s^2]$
A_Z	Acceleration in Z_b axis	$[m/s^2]$
u	Airspeed Component in X_b axis	$[m/s]$
v	Airspeed Component in Y_b axis	$[m/s]$
w	Airspeed Component in Z_b axis	$[m/s]$
δ_e	Elevator Deflection Angle	$[Rad]$
δ_a	Aileron Deflection Angle	$[Rad]$
δ_r	Rudder Deflection Angle	$[Rad]$
ν	Virtual Input	$[-]$
$\Delta(k)$	Innovation	$[-]$
K	Controller Gain	$[-]$
N	Window Length	$[-]$
σ^2	Variance	$[-]$
π_k	Auto-Correlation Function Value at k	$[-]$
λ	Forgetting Factor	$[-]$
$\hat{\Theta}$	Ordinary Least Squares Parameter Estimates	$[-]$
Constants		
S	Wing Surface Area	$[24.99\ m^2]$
b	Wing Span	$[13.325\ m]$
$\bar{c}$	Wing Chord	$[1.991\ m]$

List of Abbreviations

Abbreviation	Description
AMI	Aerodynamic Model Identification
ANDI	Adaptive Nonlinear Dynamic Inversion
INDI	Incremental Nonlinear Dynamic Inversion
NDI	Nonlinear Dynamic Inversion
OLS	Ordinary Least Squares

List of Tables

2.1 Joystick Axes Limits 2
2.2 Expected Effect of Failure on Stability and Control Derivatives 3

3.1 Estimated parameters mean, minimum, maximum & standard error values using an ordinary least squares method 6

4.1 Moving Squared Average Mean, Failure and Threshold Values 8
4.2 Variance Mean, Failure and Threshold Values 10
4.3 Auto-Correlation Pre-Failure Maximum, Failure and Threshold Values 10
4.4 Trade-Off of Statistical Metrics 11
4.5 Estimated parameters mean, minimum & maximum values using RLS with forgetting factor of $\lambda = 0.99$ 13

6.1 Moving Squared Average Mean, Failure and Threshold Values using the Manual ANDI Controller 24

List of Figures

2.1 Logitech Extreme 3D Pro Joystick . . . 2
2.2 Aileron Hardover Failure Dynamics in Actuator Block . . . 3
2.3 Body-Fixed Reference Frame [1] . . . 3

4.1 Moving Average of Squared Innovation for $N = 25$ & $N = 100$ . . . 8
4.2 Variance of Innovation . . . 9
4.3 Auto-Correlation of Innovation for $k_{gap} = 1$ & $k_{gap} = 25$, $N = 100$ & $ov = 50$ . . . 11
4.4 Innovation Values for RLS with Covariance Matrix Reset using the Moving Squared Average Metric and RLS with a Exponential Forgetting Factor of $\lambda = 0.99$ . . . 14

5.1 Aircraft Trajectory of Validation Flight with Failure using the Manual Classical Controller . . . 16
5.2 Aircraft Trajectory of Validation Flight without Failure using the Manual Classical Controller . . . 16
5.3 Control Surface Deflections & Reference Command Inputs of Validation Flight with Failure using the Manual Classical Rate Controller . . . 17
5.4 Control Surface Deflections & Reference Command Inputs of Validation Flight without Failure using the Manual Classical Rate Controller . . . 18

6.1 Structure of two-loop ANDI Controller . . . 19
6.2 Aircraft Trajectory of Validation Flight with Failure using the Manual ANDI Controller . . . 21
6.3 Aircraft Trajectory of Validation Flight without Failure using the Manual ANDI Controller . . . 21
6.4 Control Surface Deflections & Reference Command Inputs of Validation Flight with Failure using the Manual ANDI Controller . . . 22
6.5 Control Surface Deflections & Reference Command Inputs of Validation Flight without Failure using the Manual ANDI Controller . . . 23
6.6 Average Squared Innovation Metric of Validation Flights using the Manual ANDI Controller . . . 24
6.7 C_Y Stability and Control Derivative Estimates of Validation Flights using the Manual ANDI Controller . . . 25
6.8 C_l Stability and Control Derivative Estimates of Validation Flights using the Manual ANDI Controller . . . 26
6.9 C_n Stability and Control Derivative Estimates of Validation Flights using the Manual ANDI Controller . . . 27

7.1 Structure of two-loop INDI Controller . . . 29
7.2 Aircraft Trajectory of Validation Flight with Failure using the INDI Controller . . . 31
7.3 Aircraft Trajectory of Validation Flight without Failure using the INDI Controller . . . 31
7.4 Control Surface Deflections & Reference Command Inputs of Validation Flight with Failure using the Manual INDI Controller . . . 32
7.5 Control Surface Deflections & Reference Command Inputs of Validation Flight without Failure using the Manual INDI Controller . . . 33

A.1 C_X Stability and Control Derivative Estimates of Validation Flights using the Manual ANDI Controller . . . 38
A.2 C_Z Stability and Control Derivative Estimates of Validation Flights using the Manual ANDI Controller . . . 39
A.3 C_m Stability and Control Derivative Estimates of Validation Flights using the Manual ANDI Controller . . . 40

Contents

List of Tables ii

List of Figures iii

1 Introduction 1

2 Joystick Calibration & Failure Dynamics 2
- 2.1 Joystick Calibration . . . 2
- 2.2 Failure Dynamics . . . 2
  - 2.2.1 Effect on Stability & Control Derivatives . . . 3

3 AMI Algorithm 4
- 3.1 Aerodynamic Forces & Moments . . . 4
- 3.2 Aerodynamic Model Structure . . . 4
- 3.3 Ordinary Least Squares . . . 5

4 AMI Monitoring Algorithm 7
- 4.1 Statistical Metrics . . . 7
  - 4.1.1 Moving Squared Average . . . 7
  - 4.1.2 Variance . . . 9
  - 4.1.3 Auto-Correlation . . . 10
  - 4.1.4 Statistical Metrics Trade-Off . . . 11
- 4.2 RLS with Forgetting Factor . . . 12
- 4.3 RLS with Reset vs. RLS with Forgetting Factor . . . 13

5 Classical Rate Controller 15
- 5.1 Classical Rate Controller Design . . . 15
- 5.2 Validation Flights . . . 15
  - 5.2.1 Aircraft Trajectories . . . 16
  - 5.2.2 Control Surface Deflections & Reference Command Inputs . . . 17

6 ANDI Controller 19
- 6.1 ANDI Controller Design . . . 19
- 6.2 Validation Flights . . . 20
  - 6.2.1 Aircraft Trajectories . . . 21
  - 6.2.2 Control Surface Deflections & Reference Command Inputs . . . 22
  - 6.2.3 Statistical Monitoring Metric . . . 24
  - 6.2.4 Stability & Control Derivative Estimates . . . 25
  - 6.2.5 Comparison with Classical Rate Controller. . . . 28

7 INDI Controller 29
- 7.1 INDI Controller Design . . . 29
- 7.2 Validation Flights . . . 30
  - 7.2.1 Aircraft Trajectories . . . 31
  - 7.2.2 Control Surface Deflections & Reference Command Inputs . . . 32
  - 7.2.3 Comparison with ANDI & Classical Rate Controller . . . 33

8 Conclusion 35

Bibliography 36

Appendices 37

A Symmetric Control & Stability Derivative Estimates 38

1
Introduction

This document comprises the report of the Nonlinear & Adaptive Flight Control Assignment. This assignment focuses on fault tolerant control using two manual nonlinear adaptive flight controllers. An Adaptive Nonlinear Dynamic Inversion (ANDI) controller and an Incremental Nonlinear Dynamic Inversion (INDI) controller are designed and evaluated for an aileron hardover failure scenario in the provided Cessna Citation simulink model. An ANDI controller is an indirect model based control approach which involves aircraft online model identification. An INDI controller uses angular velocity measurements to obtain the angular acceleration body components which are then used in the inner-loop INDI controller.

The joystick calibration and aileron hardover failure dynamics implementation is included in chapter 2. The Aerodynamic Model Identification (AMI) algorithm which estimates the stability and control derivatives which are used online in the ANDI controller is developed in chapter 3. Several AMI monitoring algorithms which guarantee the flexibility of the AMI algorithm to the changes in the parameter estimates of the failed aircraft are analyzed in chapter 4. In chapter 5, a classical rate controller is designed and analyzed in two validation flights, with and without failure, to serve as a benchmark for the fault tolerant controllers. An ANDI controller, which uses the stability and control derivative estimates from chapter 4, is developed and tested in two validation flights in chapter 6. Finally, an INDI controller is also designed and evaluated in two validation flights in chapter 7.

2

Joystick Calibration & Failure Dynamics

2.1. Joystick Calibration

A Logitech Extreme 3D Pro joystick shown in Figure 2.1 was used to control the Cessna Citation simulation model. The joystick has 3 axes for roll, pitch & yaw in combination with a throttle lever and a large variety of buttons. In general the joystick outputs matched the control inputs to a high fidelity, however under abrupt control inputs the joystick outputs had errors when in the neutral position which disappeared with further control inputs. The calibration of the joystick was relatively straightforward, the limits used for each joystick axes are shown in Table 2.1.

Figure 2.1: Logitech Extreme 3D Pro Joystick

Table 2.1: Joystick Axes Limits

Control Channel	**Limit** [-]
δ_a	[-0.02, 0.02]
δ_e	[-0.02, 0.02]
δ_r	[-0.01, 0.01]

2.2. Failure Dynamics

The failure to be implemented is the aileron hardover failure, in which one of the ailerons deflects to a non-neutral position and gets stuck, for example, due to a hydraulics failure. The pilot will feel that the aileron channel is half as effective as before as he only has control over the remaining aileron. Furthermore, the aileron stuck in a non-neutral position will cause the aircraft to roll which has to be compensated for with the operational aileron.

The Cessna Citation simulink model does not have individual aileron channels, instead the aileron deflections are determined using Equation 2.1. The failure of one of the ailerons cannot be implemented in the simulink model directly, instead the effect of the aileron hardover failure on the aileron channel is calculated using Equation 2.2 where $\delta_{a_{\text{offset}}} = 0.28\ [rad]$ represents the angle at which the right aileron is stuck.

It is important to note that in the simulink model instead of the right aileron being stuck at an angle $\delta_{a_{\text{offset}}}$ it is approximated by the right and left ailerons being at a neutral angle of $\delta_{a_{\text{offset}}}/2$ and the aileron deflection inputs being halved.

$$\delta_{a_{\text{actual}}} = \delta_{a_{\text{leff}}} + \delta_{a_{\text{right}}} = \delta_{a_{\text{desired}}} \tag{2.1}$$

$$\begin{aligned}\delta_{a_{\text{actual}}} &= \delta_{a_{\text{left}}} + \delta_{a_{\text{offset}}} \\ &= \frac{1}{2}\delta_{a_{\text{desired}}} + \delta_{a_{\text{offset}}}\end{aligned} \tag{2.2}$$

The failure dynamics are implemented in the actuators block as shown in Figure 2.2. The failure is triggered by 2 joystick buttons that act as an on/off switch.

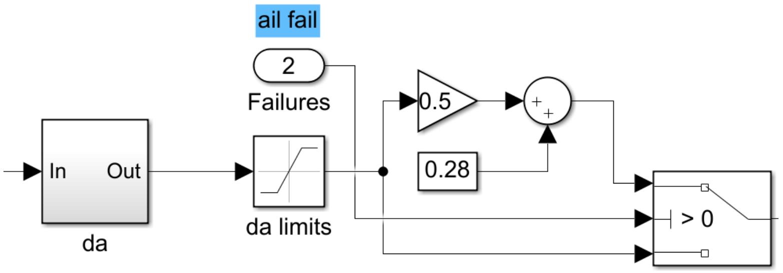

Figure 2.2: Aileron Hardover Failure Dynamics in Actuator Block

2.2.1. Effect on Stability & Control Derivatives

The aileron hardover failure will affect the asymmetric aerodynamic force and moment coefficients (C_Y, C_l & C_n). The body-fixed reference frame used along with a brief outline of the effect of the failure on the asymmetric stability and control derivatives is shown in Figure 2.3 and Table 2.2 respectively.

The failure will cause a negative change in the rolling moment stability derivative C_{l_0} since both aileron will produce a constant anti-clockwise rolling moment. In addition, the rolling moment control derivative $C_{l_{\delta_a}}$ will be halved as the aileron effectiveness to produce a rolling moment has been halved as effectively only one aileron is operational (assuming a linear relationship between aileron deflection and rolling moment).

The yawing moment stability derivative C_{n_0} will also experience a negative change as the "drag of the right wing which has the downward deflecting aileron increases, while that of the left wing decreases, or perhaps increases less" [1]. This results in a constant anti-clockwise yawing moment. It is important to note that in a real aileron hardover scenario the negative change in C_{n_0} would be greater as the drag of the failed aileron would not be counteracted by the drag of the operational aileron, resulting in a greater yawing moment. Similarly, the yawing moment control derivative $C_{n_{\delta_a}}$ will be halved as the aileron deflections are halved, thus the net drag and corresponding yawing moment produced is also halved (assuming $\delta_a \propto k \cdot M$).

Finally, the lateral stability derivative C_{Y_0} will also experience a negative change as a result of the failure. On swept wings a component of the drag caused by the ailerons acts laterally in opposite directions, the right wing has a higher drag than that of the left wing which will result in a net negative lateral force. In a real aileron hardover scenario C_{Y_0} would experience a greater negative change as the lateral force of the failed aileron would not be counteracted by that of the other aileron. The lateral control derivative $C_{Y_{\delta_a}}$ will also be halved as the net lateral force produced by the ailerons has been halved as a consequence of the aileron deflections being halved (assuming $\delta_a \propto k \cdot Y$).

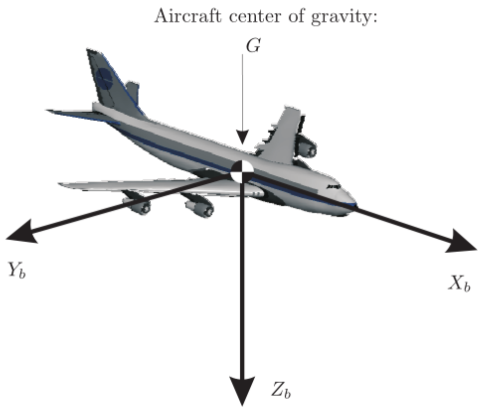

Figure 2.3: Body-Fixed Reference Frame [1]

Table 2.2: Expected Effect of Failure on Stability and Control Derivatives

	$\mathbf{C_Y}$	$\mathbf{C_l}$	$\mathbf{C_n}$
C_0	$\Delta-$	$\Delta--$	$\Delta-$
$\partial C/\partial\beta$	-	-	-
$\partial C/\partial p$	-	-	-
$\partial C/\partial r$	-	-	-
$\partial C/\partial\delta_a$	$\approx 1/2$	$\approx 1/2$	$\approx 1/2$
$\partial C/\partial\delta_r$	-	-	-

3
AMI Algorithm

Aerodynamic Model Identification (AMI) consists of estimating the aircraft's stability and control derivatives based on the aircraft's states. Typically a 2-step method is used in which first the aircraft states are estimated by making use of the kinematic and observation model, redundant but contaminated data is then passed through a Kalman Filter to obtain the estimated aircraft states. In the following step, the aerodynamic forces and moments are computed using the estimated aircraft states. A regression analysis is then performed on the aerodynamic forces and moments to estimate the stability and control derivatives.

However, for the sake of simplicity it has been assumed that the aircraft states are not contaminated and thus the aerodynamic forces and moments can be computed directly using the equations outlined in section 3.1. The stability and control derivatives of the model structure in section 3.2 are then estimated using an ordinary least squares estimator in section 3.3.

3.1. Aerodynamic Forces & Moments

The aerodynamic forces are computed using measurements of linear acceleration in the body-fixed reference frame with Equation 3.1, Equation 3.2 & Equation 3.3.

$$C_X = \frac{X}{1/2\rho V^2 S} = \frac{mA_x}{1/2\rho V^2 S} \tag{3.1}$$

$$C_Y = \frac{Y}{1/2\rho V^2 S} = \frac{mA_y}{1/2\rho V^2 S} \tag{3.2}$$

$$C_Z = \frac{Z}{1/2\rho V^2 S} = \frac{mA_z}{1/2\rho V^2 S} \tag{3.3}$$

The aerodynamic moments are calculated with measurements of angular velocity in the body-fixed reference frame along with angular accelerations which are not measured directly but instead are obtained using numerical differentiation using Equation 3.4, Equation 3.5 & Equation 3.6.

$$C_l = \frac{L}{1/2\rho V^2 Sb} = \frac{\dot{p}I_{xx} + qr\left(I_{zz} - I_{yy}\right) - (pq + \dot{r})I_{xz}}{1/2\rho V^2 Sb} \tag{3.4}$$

$$C_m = \frac{M}{1/2\rho V^2 S\bar{c}} = \frac{\dot{q}I_{yy} + rp\,(I_{xx} - I_{zz}) + \left(p^2 - r^2\right) I_{xz}}{1/2\rho V^2 S\bar{c}} \tag{3.5}$$

$$C_n = \frac{N}{1/2\rho V^2 Sb} = \frac{\dot{r}I_{zz} + pq\left(I_{yy} - I_{xx}\right) + (qr - \dot{p})I_{xz}}{1/2\rho V^2 Sb} \tag{3.6}$$

3.2. Aerodynamic Model Structure

The symmetric aerodynamic forces and moment are modeled using the stability and control derivatives in Equation 3.7, Equation 3.8 & Equation 3.9.

$$C_X = C_{X_0} + C_{X_\alpha}\alpha + C_{X_{\alpha^2}}\alpha^2 + C_{X_q}\frac{q\bar{c}}{V} + C_{X_{\delta_e}}\delta_e \tag{3.7}$$

$$C_Z = C_{Z_0} + C_{Z_\alpha}\alpha + C_{Z_q}\frac{q\bar{c}}{V} + C_{Z_{\delta_e}}\delta_e \tag{3.8}$$

$$C_m = C_{m_0} + C_{m_\alpha}\alpha + C_{m_q}\frac{q\bar{c}}{V} + C_{m_{\delta_e}}\delta_e \tag{3.9}$$

The asymmetric aerodynamic force and moments are modeled using the stability and control derivatives in Equation 3.10, Equation 3.11 & Equation 3.12.

$$C_Y = C_{Y_0} + C_{Y_\beta}\beta + C_{Y_p}\frac{pb}{2V} + C_{Y_r}\frac{rb}{2V} + C_{Y_{\delta_a}}\delta_a + C_{Y_{\delta_r}}\delta_r \tag{3.10}$$

$$C_l = C_{l_0} + C_{l_\beta}\beta + C_{l_p}\frac{pb}{2V} + C_{l_r}\frac{rb}{2V} + C_{l_{\delta_a}}\delta_a + C_{l_{\delta_r}}\delta_r \tag{3.11}$$

$$C_n = C_{n_0} + C_{n_\beta}\beta + C_{n_p}\frac{pb}{2V} + C_{n_r}\frac{rb}{2V} + C_{n_{\delta_a}}\delta_a + C_{n_{\delta_r}}\delta_r \tag{3.12}$$

The control deflections used in the identification routine are taken from the actuator block after the actuator dynamics (integrator and limit) but before the failure dynamics such that the failure does not influence the control deflections used in the identification routine. Furthermore, the yaw damper has been disabled as it cannot be included in the identified model.

3.3. Ordinary Least Squares

The principles of regression analysis in the framework of aerodynamic model identification are well known [2]. For each of the equations in section 3.2 substituting force of moment coefficient values computed in section 3.1 on the left side along with the corresponding measured aircraft states and controls on the right side results in an over-determined set of equations for the stability and control derivatives. The unknown stability and control derivatives are estimated using the ordinary least squares (OLS) method shown in Equation 3.13.

$$\mathbf{y} = \mathbf{X}\hat{\Theta} + \boldsymbol{\nu} \tag{3.13}$$

The OLS estimator finds the optimal $\hat{\Theta}$ values by minimizing the sum S of squared residuals between the computed aerodynamic forces and moments and the aerodynamic model shown in Equation 3.14.

$$S = \frac{1}{2}(\mathbf{y} - \mathbf{X}\hat{\Theta})^T(\mathbf{y} - \mathbf{X}\hat{\Theta}) \tag{3.14}$$

Solving for the estimated parameters gives the closed form solution in Equation 3.15.

$$\hat{\Theta} = \left(\mathbf{X}^\top\mathbf{X}\right)^{-1}\mathbf{X}^\top\mathbf{y} \tag{3.15}$$

The estimated parameters covariance matrix is computed using Equation 3.16 [3] where n_p is the amount of estimated parameters. The standard error of the estimated parameters are given by the square root of the diagonal elements of the covariance matrix.

$$\begin{aligned} \mathrm{Cov}(\hat{\Theta}) &\equiv E\left[(\hat{\Theta} - \Theta)(\hat{\Theta} - \Theta)^T\right] \\ &= \hat{\sigma}^2\left(\boldsymbol{X}^T\boldsymbol{X}\right)^{-1} \end{aligned} \tag{3.16}$$

$$\hat{\sigma}^2 = \frac{(\mathbf{y} - \mathbf{X}\hat{\Theta})^T(\mathbf{y} - \mathbf{X}\hat{\Theta})}{\left(N - n_p\right)} \tag{3.17}$$

Since the OLS estimates are used in a real-time application it is more computationally efficient to update the estimates recursively, as new data becomes available following the recursive form:

$$L(k) = P(k-1)X(k)\left(X(k)^T P(k-1)X(k) + 1\right)^{-1} \tag{3.18}$$

$$\hat{\Theta}(k) = \hat{\Theta}(k-1) + L(k)\left(y(k) - X(k)^T\hat{\Theta}(k-1)\right) \tag{3.19}$$

$$P(k) = \left(I - L(k)X(k)^T\right)P(k-1) \tag{3.20}$$

For example, for the recursive least squares (RLS) method on the pitching moment coefficient C_m we have

- $y(k)$ the pitching moment coefficient C_m at iteration k computed with Equation 3.5
- $X(k)$ a 4 × 1 vector containing the aircraft states and controls from Equation 3.9 at iteration k

$$X(k) = \begin{bmatrix} 1 & \alpha(k) & \frac{q(k)\bar{c}}{V(k)} & \delta_e(k) \end{bmatrix}^T$$

- $\hat{\Theta}(k)$ a 1×4 vector containing the estimates for the stability and control derivatives from Equation 3.9 at iteration k with initial value $\hat{\Theta}(k_0)$

$$\hat{\Theta}(k) = \begin{bmatrix} C_{m_0} & C_{m_\alpha} & C_{m_q} & C_{m_{\delta_e}} \end{bmatrix}$$

$$\hat{\Theta}(k_0) = \begin{bmatrix} 0 & -0.1 & -4 & -0.2 \end{bmatrix}$$

- $P(k)$ a 4×4 covariance matrix at iteration k with initial value $P(k_0)$

$$P(k_0) = \begin{pmatrix} 10000 & 0 & \cdots & 0 \\ 0 & 10000 & \cdots & 0 \\ \vdots & \vdots & \ddots & \vdots \\ 0 & 0 & \cdots & 10000 \end{pmatrix}$$

The mean, maximum, minimum and standard error of the stability and control derivative estimates obtained using an RLS method during $T = 10 - 120$ $[s]$ of a flight are shown in Table 3.1. The OLS method performs well at estimating the stability and control derivatives with a low standard error with a few exceptions: the pitch rate stability derivatives $\partial C / \partial q$ and the angle of attack stability derivatives: C_{X_α} & $C_{X_{\alpha^2}}$.

Table 3.1: Estimated parameters mean, minimum, maximum & standard error values using an ordinary least squares method

Symmetric					**Asymmetric**				
	$\overline{\Theta}$ $[-]$	$\hat{\Theta}_{\mathbf{min}}$ [-]	$\hat{\Theta}_{\mathbf{max}}$ [-]	**SE** $[-]$		$\overline{\Theta}$ $[-]$	$\hat{\Theta}_{\mathbf{min}}$ $[-]$	$\hat{\Theta}_{\mathbf{max}}$ $[-]$	**SE** $[-]$
$\mathbf{C_X}$					$\mathbf{C_Y}$				
$\mathbf{C_{X_0}}$	0.021	-0.036	0.037	$1.59 \cdot 10^{-4}$	C_{Y_0}	0.000	0.000	0.000	$1.79 \cdot 10^{-5}$
$\mathbf{C_{X_\alpha}}$	-0.447	-0.925	1.065	0.018	$\mathbf{C_{Y_\beta}}$	-0.761	-0.775	-0.739	$2.16 \cdot 10^{-3}$
$\mathbf{C_{X_{\alpha^2}}}$	7.667	-6.354	10.539	0.307	$\mathbf{C_{Y_p}}$	-0.093	-0.180	-0.014	$9.32 \cdot 10^{-3}$
$\mathbf{C_{X_q}}$	-15.379	-26.774	-10.372	0.223	$\mathbf{C_{Y_r}}$	0.795	0.711	0.864	$8.30 \cdot 10^{-3}$
$\mathbf{C_{X_{\delta_e}}}$	-1.268	-2.383	-1.052	0.015	$\mathbf{C_{Y_{\delta_a}}}$	-0.055	-0.081	-0.010	$3.42 \cdot 10^{-3}$
					$\mathbf{C_{Y_{\delta_r}}}$	0.200	0.184	0.233	$1.17 \cdot 10^{-3}$
$\mathbf{C_Z}$					$\mathbf{C_l}$				
$\mathbf{C_{Z_0}}$	-0.138	-0.139	-0.135	$3.48 \cdot 10^{-5}$	$\mathbf{C_{l_0}}$	0.000	0.000	0.000	$6.92 \cdot 10^{-7}$
$\mathbf{C_{Z_\alpha}}$	-5.652	-5.677	-5.567	$3.07 \cdot 10^{-3}$	$\mathbf{C_{l_\beta}}$	-0.101	-0.102	-0.098	$8.32 \cdot 10^{-5}$
$\mathbf{C_{Z_q}}$	-9.616	-10.717	-6.857	0.063	$\mathbf{C_{l_p}}$	-0.457	-0.466	-0.438	$3.59 \cdot 10^{-4}$
$\mathbf{C_{Z_{\delta_e}}}$	-0.736	-0.787	-0.600	$4.24 \cdot 10^{-3}$	$\mathbf{C_{l_r}}$	0.157	0.155	0.160	$3.20 \cdot 10^{-4}$
					$\mathbf{C_{l_{\delta_a}}}$	-0.184	-0.185	-0.183	$1.32 \cdot 10^{-4}$
					$\mathbf{C_{l_{\delta_r}}}$	0.034	0.032	0.035	$4.49 \cdot 10^{-5}$
$\mathbf{C_m}$					$\mathbf{C_n}$				
$\mathbf{C_{m_0}}$	0.006	0.004	0.013	$4.75 \cdot 10^{-5}$	$\mathbf{C_{n_0}}$	0.000	0.000	0.000	$5.51 \cdot 10^{-7}$
$\mathbf{C_{m_\alpha}}$	-0.681	-0.787	-0.597	$4.18 \cdot 10^{-3}$	$\mathbf{C_{n_\beta}}$	0.143	0.142	0.145	$6.63 \cdot 10^{-5}$
$\mathbf{C_{m_q}}$	-5.082	-6.385	-2.697	0.086	$\mathbf{C_{n_p}}$	-0.055	-0.061	-0.051	$2.86 \cdot 10^{-4}$
$\mathbf{C_{m_{\delta_e}}}$	-0.894	-1.008	-0.732	$5.77 \cdot 10^{-3}$	$\mathbf{C_{n_r}}$	-0.211	-0.215	-0.189	$2.55 \cdot 10^{-4}$
					$\mathbf{C_{n_{\delta_a}}}$	-0.011	-0.012	-0.009	$1.04 \cdot 10^{-4}$
					$\mathbf{C_{n_{\delta_r}}}$	-0.097	-0.097	-0.093	$3.57 \cdot 10^{-5}$

Aircraft parameter estimation is often associated with data collinearity [3] leading to errors in the estimated parameters of the RLS method. The accuracy of the estimated parameters could be further increased in the case of multi-collinearity by instead using a Principal Components Regression method.

4
AMI Monitoring Algorithm

The RLS method assumes that the true parameter values (Θ) remain constant, while under normal flying conditions this a suitable assumption, it is not when a failure occurs. To ensure flexibility of the RLS algorithm to varying parameters values the use of a forgetting factor λ has been analysed in section 4.2. Another option is the use of statistical monitoring metrics investigated in section 4.1 to trigger a reset of the covariance matrix P_k to its initial diagonal structure to ensure that the gradually "frozen" estimated parameters are free to change.

The performance of the RLS method at estimating the parameter values is analysed with the innovation of the estimated aerodynamic model for each force and moment coefficient shown in Equation 4.1.

$$\Delta(k) = y(k) - X(k)\hat{\Theta}_{RLS}(k) \tag{4.1}$$

4.1. Statistical Metrics

A total of 3 statistical metrics are analysed: moving squared average, variance and auto-correlation. The values of the statistical metrics for a conventional flight are shown and analysed. During the first few seconds of the RLS parameter estimates they are "melted" from their initial guesses which result in large innovation values. To prevent false positives in the statistical metrics the first 10 seconds of the simulation are not analysed. The statistical metrics are then compared in a trade-off to determine which metric to use in the monitoring algorithm.

The resetting thresholds are determined individually for the six separate force and moment coefficients. If a failure is detected in one of the symmetric (C_X, C_Z, C_m) or asymmetric coefficients (C_Y, C_l, C_n) this will trigger a reset of the covariance matrix of all the corresponding symmetric or asymmetric coefficients.

4.1.1. Moving Squared Average

The moving average of the squared innovation was determined with Equation 4.2 where N is the window length over which the moving average is computed.

$$\bar{\Delta}(k) = \frac{1}{N}\sum_{i=0}^{N}\Delta(k-i)^2 \tag{4.2}$$

The moving average of the squared innovation for window sizes $N = 25$ & $N = 100$ are shown in Figure 4.1.

The aileron hardover failure causes the largest peak for the moving average of the squared innovation in C_l, smaller peaks are also noticeable in the other asymmetric coefficients (C_Y & C_n). During cruise flight with no control inputs, marked by the green area in Figure 4.1, the moving average is generally smoother and smaller than under normal flying conditions as the aerodynamic model is better able to predict the force and moment coefficients acting on the aircraft.

A narrower window size makes the peaks at the failure larger and thus easier to detect, however this comes at the cost of a more noisy moving average signal. To ensure that the aileron hardover failure is detected and false positives are avoided a high magnitude of the C_l failure peak is desired but with a low pre-failure maximum. A window size of $N = 25$ is chosen as it has a larger ratio of the C_l failure peak to the maximum before the failure.

The aileron hardover failure considered only affects the asymmetric force and moment coefficients, specifically the C_l coefficient. To determine the moving squared average thresholds for all coefficients to trigger the

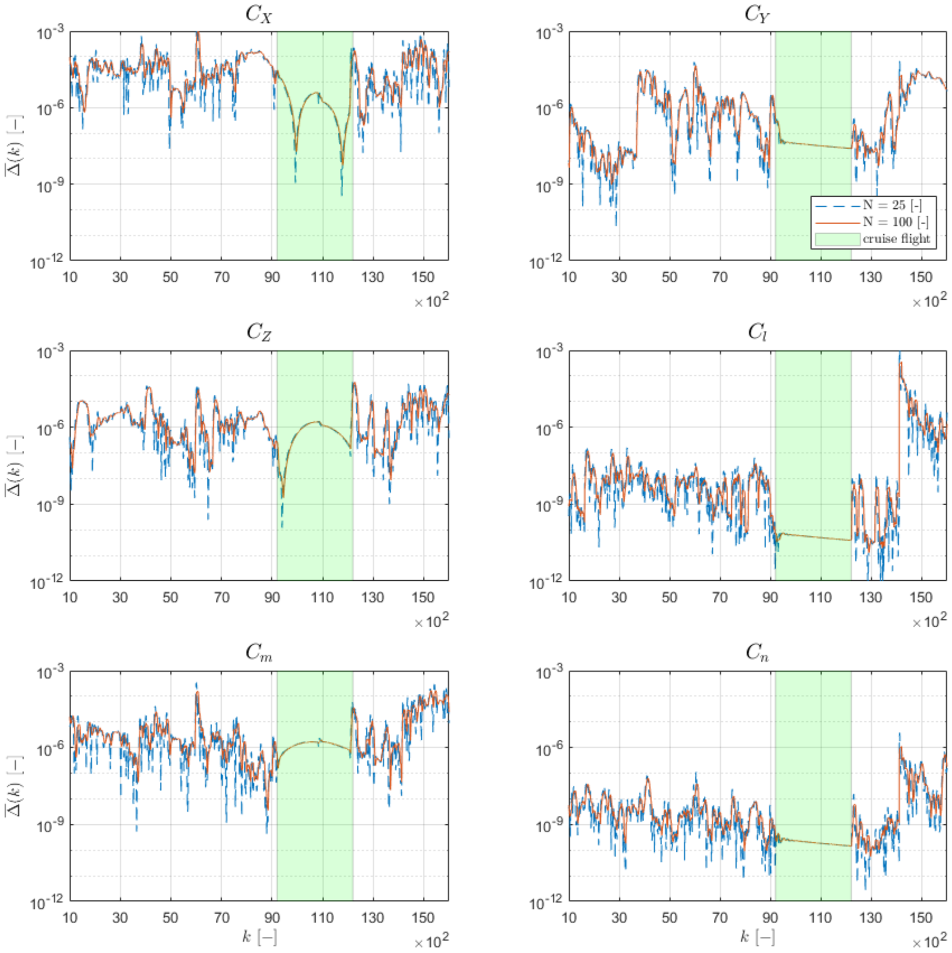

Figure 4.1: Moving Average of Squared Innovation for $N = 25$ & $N = 100$

reset of the covariance matrix P_k further analysis of other failure modes and severities should be performed. Instead for the sake of this practical, it has been assumed that the magnitude of the moving squared average of C_l at failure relative to the pre-failure C_l maximum value is representative of other failure modes for other coefficients. A moving squared average threshold in the midpoint between the failure peak and the pre-failure maximum value proved suitable for detecting the failure but avoiding false positives. The moving squared average pre-failure maximum, failure peak and threshold values used are shown in Table 4.1.

Table 4.1: Moving Squared Average Mean, Failure and Threshold Values

Coefficients	$\overline{\Delta}(\mathbf{k})_{\mathbf{max}}$ [−]	$\overline{\Delta}(\mathbf{k})_{\mathbf{fail}}$ [−]	$\overline{\Delta}(\mathbf{k})_{\mathbf{thr}}$ [−]
$\mathbf{C_X}$	$1.88 \cdot 10^{-3}$	-	7.247
$\mathbf{C_Y}$	$6.89 \cdot 10^{-6}$	-	0.266
$\mathbf{C_m}$	$3.43 \cdot 10^{-6}$	-	1.322
$\mathbf{C_Y}$	$6.01 \cdot 10^{-6}$	$6.60 \cdot 10^{-5}$	0.232
$\mathbf{C_l}$	$1.60 \cdot 10^{-8}$	$1.24 \cdot 10^{-3}$	$6.18 \cdot 10^{-4}$
$\mathbf{C_n}$	$1.12 \cdot 10^{-9}$	$3.74 \cdot 10^{-6}$	$4.32 \cdot 10^{-4}$

4.1.2. Variance

The variances of the innovation is computed using Equation 4.3.

$$\sigma^2_\Delta(k) = \frac{1}{N-1}\sum_{k=1}^{N}(\Delta(k)-\bar{\Delta})^2 \quad \text{with:} \quad \bar{\Delta} = \frac{1}{N}\sum_{k=1}^{N}\Delta(k) \tag{4.3}$$

The variances of the innovations of the force and moment coefficients are shown in Figure 4.2.

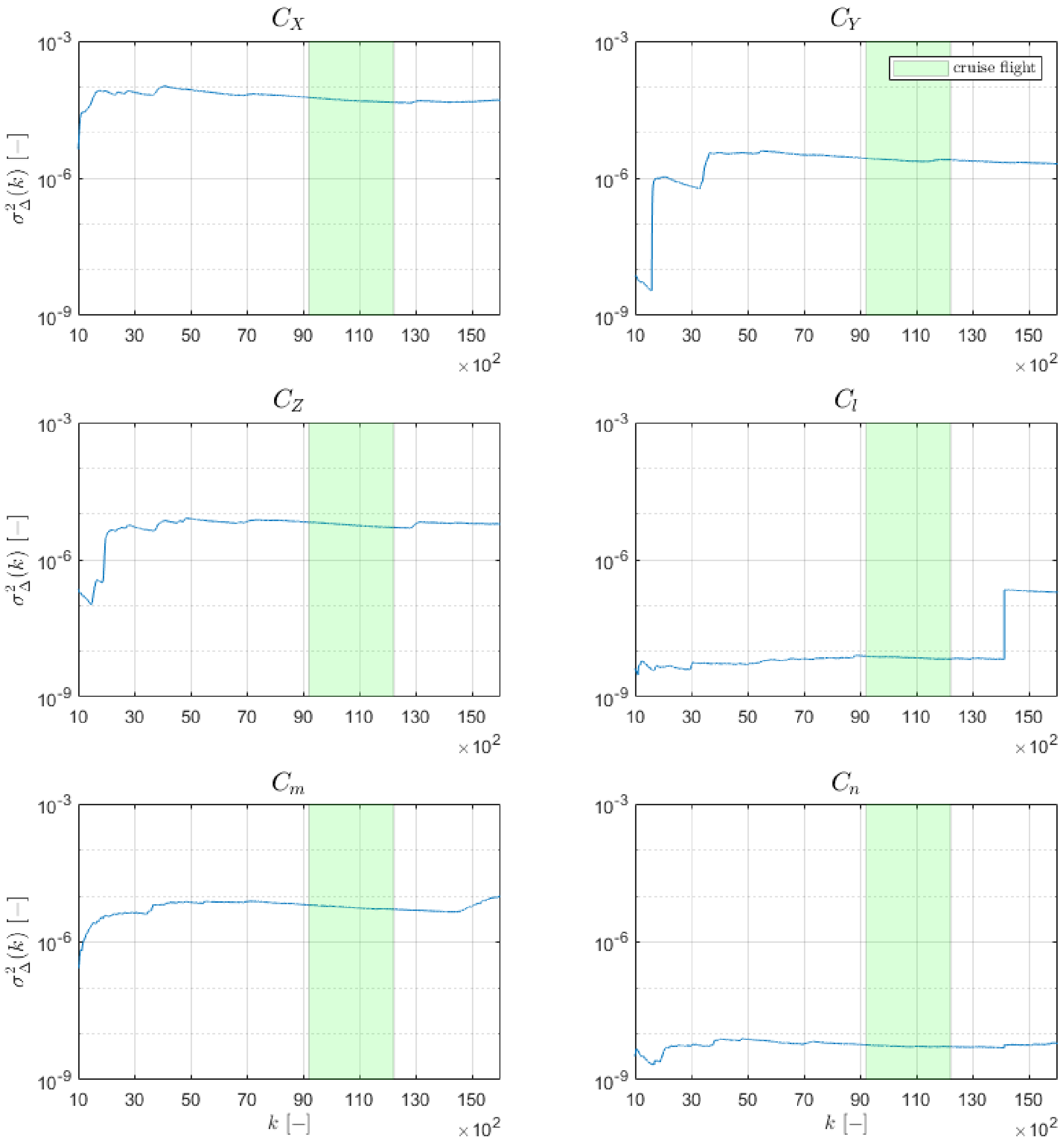

Figure 4.2: Variance of Innovation

The aileron hardover failure causes a significant increase in the variance of C_l caused by large innovation values, which is also observed by the large failure peak in the C_l moving squared average. After the failure the variance retains it's increased value, to ensure that additional failures are detected the variance of the affected coefficients should be reset. The failure is barely noticeable in the C_Y & C_n variances. During cruise flight the variance of the innovations slowly decrease due to a better aerodynamic model fidelity.

The variance is computed over the entire innovation values unlike the moving squared average which is computed over a moving window size. The smoother variances might seem preferable over the moving squared averages, however the effect of the failure on the variance will vary depending on the amount of innovation values over which the variance is computed. A failure at 10 seconds will cause a greater increase in the variance than the same failure at 1000 seconds, since the time when the failure occurs should be inherently unknown computing the variance over the entire innovation values is undesirable. Furthermore, there is a risk of the variance creeping up, for example, due to severe turbulence and triggering a false positive.

The variance thresholds to trigger the reset of the covariance matrix P_k are shown in Table 4.2 are determined using the same method as those of the moving squared average.

Table 4.2: Variance Mean, Failure and Threshold Values

Coefficients	$\sigma^{\mathbf{2}}_{\Delta}(\mathbf{k})_{\mathbf{max}}$ [−]	$\sigma^{\mathbf{2}}_{\Delta}(\mathbf{k})_{\mathbf{fail}}$ [−]	$\sigma^{\mathbf{2}}_{\Delta}(\mathbf{k})_{\mathbf{thr}}$ [−]
$\mathbf{C_X}$	$1.03 \cdot 10^{-4}$	-	$1.41 \cdot 10^{-3}$
$\mathbf{C_Y}$	$8.09 \cdot 10^{-6}$	-	$1.11 \cdot 10^{-4}$
$\mathbf{C_m}$	$7.59 \cdot 10^{-6}$	-	$1.03 \cdot 10^{-4}$
$\mathbf{C_Y}$	$3.95 \cdot 10^{-6}$	$2.21 \cdot 10^{-6}$	$5.39 \cdot 10^{-5}$
$\mathbf{C_l}$	$8.02 \cdot 10^{-9}$	$2.19 \cdot 10^{-7}$	$1.09 \cdot 10^{-7}$
$\mathbf{C_n}$	$7.81 \cdot 10^{-9}$	$5.77 \cdot 10^{-9}$	$1.07 \cdot 10^{-7}$

4.1.3. Auto-Correlation

The auto-correlation function for a given k_{gap} is computed using Equation 4.4, where N is the window length over which the auto-correlation is computed and ov is the overlap between windows.

$$\pi_{k_{\text{gap}}} = \frac{1}{N} \sum_{t=0}^{N-k_{\text{gap}}} \Delta(t)\Delta\left(t+k_{\text{gap}}\right) \tag{4.4}$$

The auto-correlation of the innovation for $k_{gap} = 1$ & $k_{gap} = 25$, $N = 100$ & $ov = 50$ is shown in Figure 4.3.

The failure causes large innovation values in the asymmetric coefficients which create a large peak in the auto-correlation value of C_l and smaller but observable peaks in the C_Y & C_n coefficients. During cruise flight the auto-correlation values remain relatively steady due to the higher fidelity of the aerodynamic model with results in smaller innovation values.

A larger value of k_{gap} reduces the auto-correlation values as the innovation will have less in common with itself the further in time it is compared to. To determine which k_{gap} value is best suited for failure detection the same methodology used in the moving squared average has been used, where a high failure magnitude and a low pre-failure maximum are desired. A $k_{gap} = 1$ is chosen as it has a larger ratio between the failure peak and the pre-failure maximum.

The auto-correlation, unlike the other statistical metrics analysed, is not "continuous" signal. The auto-correlation is computed over a window of innovation values, the window must first be filled with either the overlap of the previous window or new innovation values before the auto-correlation is computed. The failure detection would be delayed as a consequence of the discrete nature of the auto-correlation in comparison to the other statistical metrics. Furthermore, the computation of the auto-correlation is generally more computationally intensive than the computations of the other statistical metrics.

The auto-correlation thresholds to trigger the reset of the covariance matrix P_k are shown in Table 4.3 are determined using the same method as those of the moving squared average.

Table 4.3: Auto-Correlation Pre-Failure Maximum, Failure and Threshold Values

Coefficients	$\pi_{\mathbf{1}}(\mathbf{k})_{\mathbf{max}}$ [−]	$\pi_{\mathbf{1}}(\mathbf{k})_{\mathbf{fail}}$ [−]	$\pi_{\mathbf{1}}(\mathbf{k})_{\mathbf{thr}}$ [−]
$\mathbf{C_X}$	$3.27 \cdot 10^{-4}$	-	0.318
$\mathbf{C_Y}$	$1.91 \cdot 10^{-5}$	-	0.019
$\mathbf{C_m}$	$1.67 \cdot 10^{-5}$	-	0.016
$\mathbf{C_Y}$	$1.45 \cdot 10^{-5}$	$3.26 \cdot 10^{-5}$	0.014
$\mathbf{C_l}$	$7.81 \cdot 10^{-8}$	$1.52 \cdot 10^{-4}$	$7.61 \cdot 10^{-5}$
$\mathbf{C_n}$	$3.47 \cdot 10^{-8}$	$5.87 \cdot 10^{-7}$	$3.38 \cdot 10^{-5}$

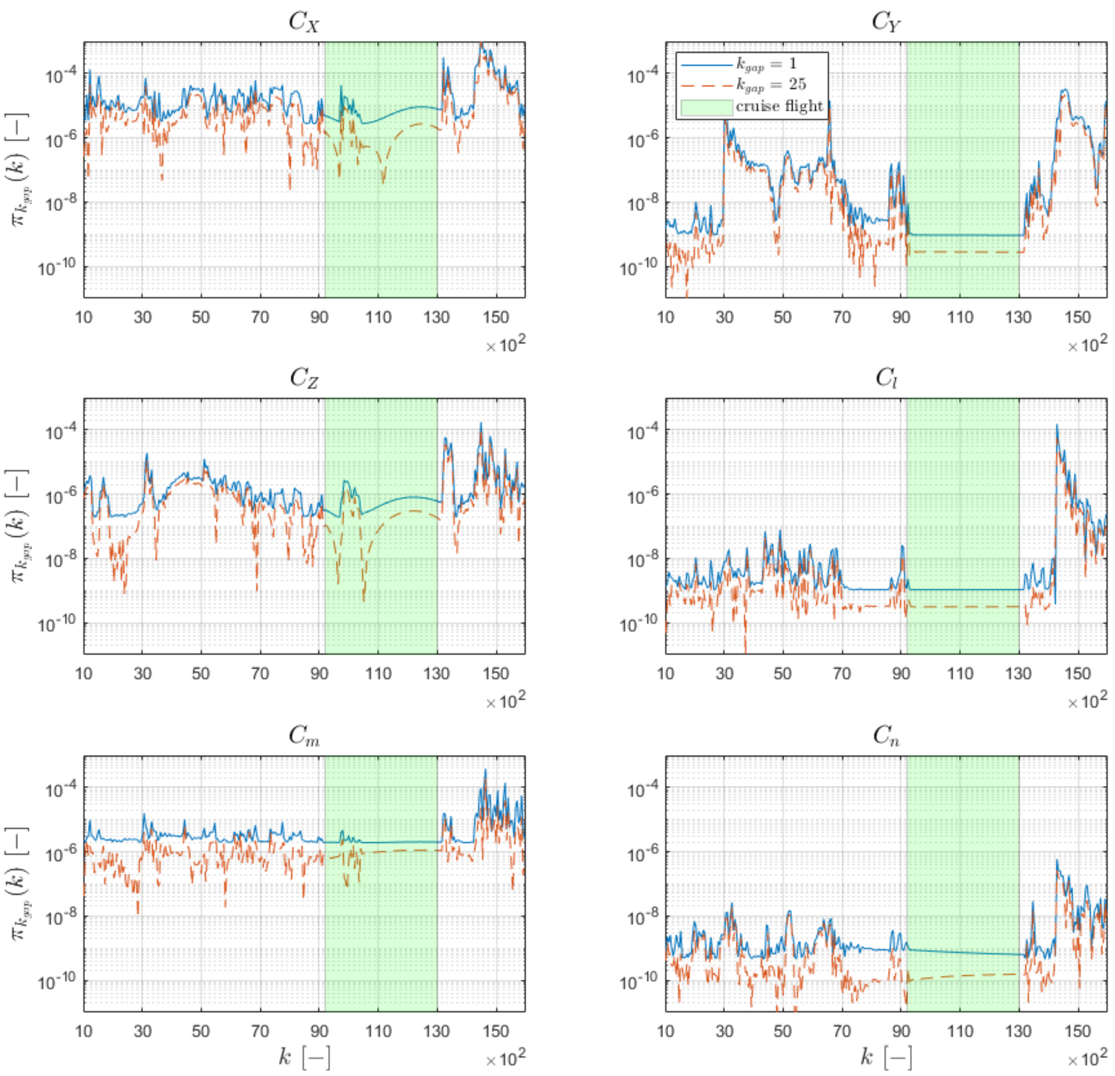

Figure 4.3: Auto-Correlation of Innovation for $k_{gap} = 1$ & $k_{gap} = 25$, $N = 100$ & $ov = 50$

4.1.4. Statistical Metrics Trade-Off

A trade-off of the statistical metrics analysed in section 4.1 is performed in Table 4.4 in order to determine which one is best suited for the AMI monitoring algorithm. The statistical metrics have been ranked in three different criteria: performance, versatility & computational complexity. The moving squared average is the chosen statistical metric as it scored the highest in the trade-off.

Table 4.4: Trade-Off of Statistical Metrics

	Performance	**Versatility**	**Computational Complexity**	**Score**
Moving Squared Average	Medium	High	Low	**8**
Variance	High	Low	Medium	**6**
Auto-Correlation	Medium	Medium	High	**6**

The ability of the statistical metrics at identifying the failure and discarding false alarms is measured in the performance criteria. All statistical metrics where able to successfully detect the failure under normal flying conditions, however the variance ranks highest in the performance criteria due to it's lower susceptibility to false alarms. The other metrics struggled more to distinguish a failure from extreme flying conditions such as abrupt pilot inputs or stall conditions.

The capability of the statistical metrics to adapt to varying failure conditions is measured in the versatility criteria. The effect of the failure on the moving squared average is only dependant on the moving window length, therefore it scores the highest in the versatility criteria. The variance scores the lowest in the versatility criteria due to the influence of the failure timing on the increase of the variance which could result in the failure being undetected if it occurs after a long period of time. Finally, the auto-correlation has a medium score in the versatility criteria due to the influence of the window size and overlap on the failure detection in addition to the slight delay in the detection of the a failure due to the use of $\Delta(t + k_{\text{gap}})$ in the auto-correlation computation.

The resources used by the the various statistical metrics are ranked in the computational complexity criteria. The moving squared average is a simple computation irrespective of the flight duration, thus it ranks lowest in the computational complexity criteria. The variance computation is performed recursively which requires few computational resources, however long flights could cause overflow issues in the variance computation, therefore it has a medium score in the computational complexity criteria. The auto-correlation has the highest computational complexity score as it requires the most computational resources in both storing data and computing the auto-correlation values.

4.2. RLS with Forgetting Factor

If the parameter values of the RLS method vary a forgetting factor λ with a value $0 < \lambda \leq 1$ can be implemented which exponentially diminishes the weight of more remote data on the calculation of the parameter estimates.

This is known as a recursive least squares with exponential forgetting scheme which is computed using the same Equation 3.19 for $\hat{\Theta}(k)$ as in the RLS scheme but with $L(K)$ and $P(k)$ computed using Equation 4.5 and Equation 4.6 respectively.

$$L(k) = P(k-1)X(k)\left(X(k)^T P(k-1)X(k) + \lambda\right)^{-1} \tag{4.5}$$

$$P(k) = \frac{1}{\lambda}\left(I - L(k)X(k)^T\right)P(k-1) \tag{4.6}$$

The main difference with the RLS method is how the covariance matrix $P(k)$ is updated. In the RLS method the covariance vanishes to zero with time losing its capability to keep track of time-varying parameter values, whereas in the "RLS with exponential forgetting the covariance matrix is divided by $\lambda < 1$ at each update which slows down the fading of the covariance matrix" [4].

"The RLS with forgetting factor has been widely used in the estimation and tracking of time-varying parameters in various fields of engineering" [4]. "Rigorous mathematical analysis of the tracking capabilities of the estimator when the parameters are time-varying is rare in literature, however in general exponential convergence in the constant case implies a certain degree of tracking capability in the time-varying case" [5].

When there is poor excitation in the system, for example during cruise flight, old information is gradually forgotten while there is little new dynamic information from which to estimate the parameters. This might lead to a covariance "wind-up" where the covariance matrix exponentially grows and as a result the estimations becomes extremely sensitive and therefore susceptible to aerodynamic model and computational errors.

A high forgetting factor is desired during cruise flight conditions such that the estimated parameters remain within reasonable bounds, however a low forgetting factor is desired when a failure occurs such that the new parameters are quickly identified. A forgetting factor of $\lambda = 0.99$ reasonably meet both considerations, however perhaps a time-varying forgetting factor is more suitable and should be investigated. Another consideration to be investigated is limiting the growth of the covariance matrix, for example by using an upper bound.

The mean, maximum and minimum of the stability and control derivative estimates obtained using an RLS with an exponential forgetting factor of $\lambda = 0.99$ during $T = 10 - 120$ $[s]$ of a flight are shown in Table 4.5.

Table 4.5: Estimated parameters mean, minimum & maximum values using RLS with forgetting factor of $\lambda = 0.99$

Symmetric				**Asymmetric**			
	$\overline{\Theta}$ [−]	$\hat{\Theta}_{\mathbf{min}}$ [−]	$\hat{\Theta}_{\mathbf{max}}$ [−]		$\overline{\Theta}$ [−]	$\hat{\Theta}_{\mathbf{min}}$ [−]	$\hat{\Theta}_{\mathbf{max}}$ [−]
$\mathbf{C_X}$				$\mathbf{C_Y}$			
$\mathbf{C_{X_0}}$	0.020	-0.140	0.094	$\mathbf{C_{Y_0}}$	0.000	-0.010	0.010
$\mathbf{C_{X_\alpha}}$	0.359	-9.252	5.771	$\mathbf{C_{Y_\beta}}$	-0.745	-0.871	-0.648
$\mathbf{C_{X_{\alpha^2}}}$	-6.327	-224.667	203.264	$\mathbf{C_{Y_p}}$	0.013	-0.444	0.422
$\mathbf{C_{X_q}}$	-3.795	-44.116	5.644	$\mathbf{C_{Y_r}}$	0.871	0.265	1.560
$\mathbf{C_{X_{\delta_e}}}$	-0.221	-4.813	0.429	$\mathbf{C_{Y_{\delta_a}}}$	-0.038	-0.192	0.088
				$\mathbf{C_{Y_{\delta_r}}}$	0.184	0.060	0.234
$\mathbf{C_Z}$				$\mathbf{C_l}$			
$\mathbf{C_{Z_0}}$	-0.136	-0.143	-0.123	$\mathbf{C_{l_0}}$	0.000	0.000	0.000
$\mathbf{C_{Z_\alpha}}$	-5.775	-6.655	-5.456	$\mathbf{C_{l_\beta}}$	-0.101	-0.107	-0.088
$\mathbf{C_{Z_q}}$	-5.933	-16.566	3.356	$\mathbf{C_{l_p}}$	-0.458	-0.495	-0.393
$\mathbf{C_{Z_{\delta_e}}}$	-0.603	-1.638	-0.083	$\mathbf{C_{l_r}}$	0.157	0.139	0.211
				$\mathbf{C_{l_{\delta_a}}}$	-0.184	-0.189	-0.156
				$\mathbf{C_{l_{\delta_r}}}$	0.035	0.029	0.044
$\mathbf{C_m}$				$\mathbf{C_n}$			
$\mathbf{C_{m_0}}$	0.007	-0.007	0.031	$\mathbf{C_{n_0}}$	0.000	0.000	0.000
$\mathbf{C_{m_\alpha}}$	-0.866	-2.839	-0.025	$\mathbf{C_{n_\beta}}$	0.143	0.127	0.156
$\mathbf{C_{m_q}}$	-2.809	-12.260	16.336	$\mathbf{C_{n_p}}$	-0.052	-0.130	0.006
$\mathbf{C_{m_{\delta_e}}}$	-0.909	-2.321	0.223	$\mathbf{C_{n_r}}$	-0.204	-0.252	-0.144
				$\mathbf{C_{n_{\delta_a}}}$	-0.010	-0.041	-0.002
				$\mathbf{C_{n_{\delta_r}}}$	-0.097	-0.103	-0.085

The mean values of the estimated parameters are similar to those obtained using the RLS method which indicates a suitable degree of tracking capability of the RLS with forgetting factor of $\lambda = 0.99$ method. However, the maximum and minimum values of the estimated parameters are significantly larger than those obtained in the RLS method, either due to effectively performing the parameter estimation on a small sample of data or covariance matrix "wind-up" during cruise flight conditions.

4.3. RLS with Reset vs. RLS with Forgetting Factor

The moving average innovation values of the RLS with covariance matrix reset method and RLS with forgetting factor method are shown in Figure 4.4.

The RLS with an exponential forgetting factor of $\lambda = 0.99$ has lower innovation values, specially during cruise flight conditions, due to the parameters being estimated based on recent data. However, as seen in Table 4.5 the range of estimated parameter values is significantly larger for the RLS with forgetting factor than that of the RLS estimated parameter values shown in Table 3.1. The moving squared average metric correctly detected the failure triggering the covariance matrix reset of the asymmetric coefficients without any false positives. The RLS with covariance matrix reset reached normal innovation values directly after the failure, indicating that the new parameter values have been quickly estimated. On the other hand, the RLS with forgetting factor method was significantly slower at estimating the new parameter values due to previous data before the failure influencing the parameter estimates after the failure.

The RLS with covariance matrix reset is preferred as it is capable of tracking abrupt changes in the parameter values, which is the case after the failure. The RLS with forgetting factor is better suited for slow changes in the parameter values. The lower innovation values of the RLS with forgetting factor do not outweigh the greater range of parameter estimates and the slower tracking of the parameter values after the failure.

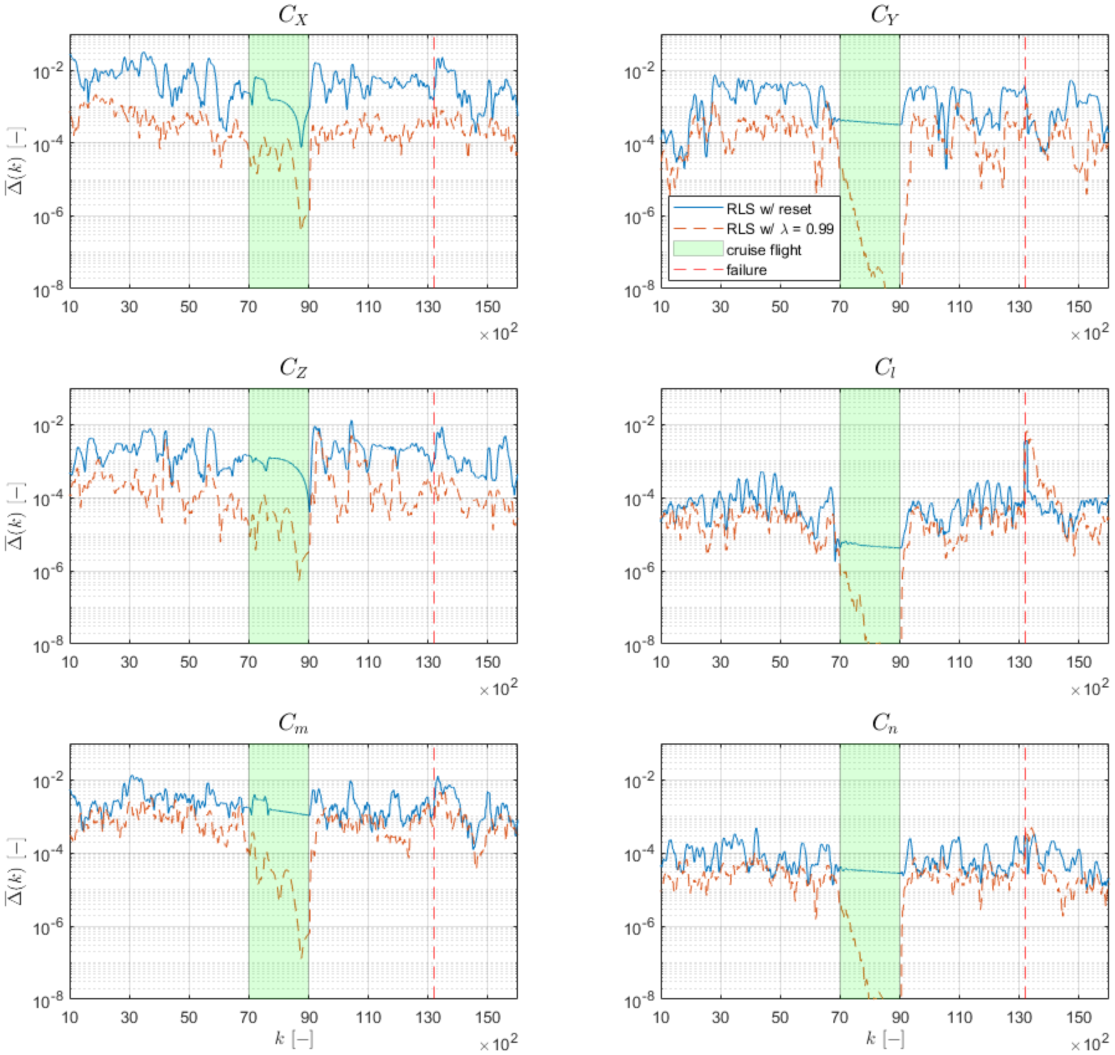

Figure 4.4: Innovation Values for RLS with Covariance Matrix Reset using the Moving Squared Average Metric and RLS with a Exponential Forgetting Factor of $\lambda = 0.99$

5
Classical Rate Controller

A manual classical rate controller is designed for the Cessna Citation simulink model to serve as a benchmark to compare the ANDI controller from chapter 6 and the INDI controller from chapter 7.

The design of the classical rate controller is described in section 5.1. The data of two validation flights, one with failure and one without, using the classical rate controller to control the Cessna Citation simulink model is shown and analyzed in section 5.2.

5.1. Classical Rate Controller Design

The control inputs of the classical rate controller are the reference angular rates p_{ref}, q_{ref} & r_{ref} supplied by the joystick. Sideslip feedback is included in the yaw rate channel to prevent dutch roll oscillations, the yaw rate is then passed through a PI controller with gains $K_{P_\beta} = -1$ and $K_{I_\beta} = -0.1$. Angular rate feedback is then introduced in the respective channel along with PI controllers with the following gains:

- Pitch Rate: $K_{P_p} = -1$ and $K_{I_p} = -0.5$
- Roll Rate: $K_{P_q} = -2$ and $K_{I_p} = -0.01$
- Yaw Rate: $K_{P_r} = -1$ and $K_{I_r} = -0.5$

5.2. Validation Flights

The classical rate controller has been used to fly the Cessna Citation simulink model in two validation flights, one with failure and one without. The data of the validation flights is shown and analyzed in this section. The aircraft trajectories of the two validation flights are shown in subsection 5.2.1. The time histories of the control surface deflection along with the reference command inputs supplied by the joystick are shown and analyzed in subsection 5.2.2.

5.2.1. Aircraft Trajectories

The aircraft trajectories of the validation flights with and without failure are shown in Figure 5.1 and Figure 5.2 respectively.

The aircraft trajectories of both validation flights closely follow the validation trajectory example provided, however the turns are slightly tighter. There are no significant differences between the aircraft trajectories of the two validation flights apart from the turns of the validation flight with failure being slightly more aggressive than those of the validation without failure.

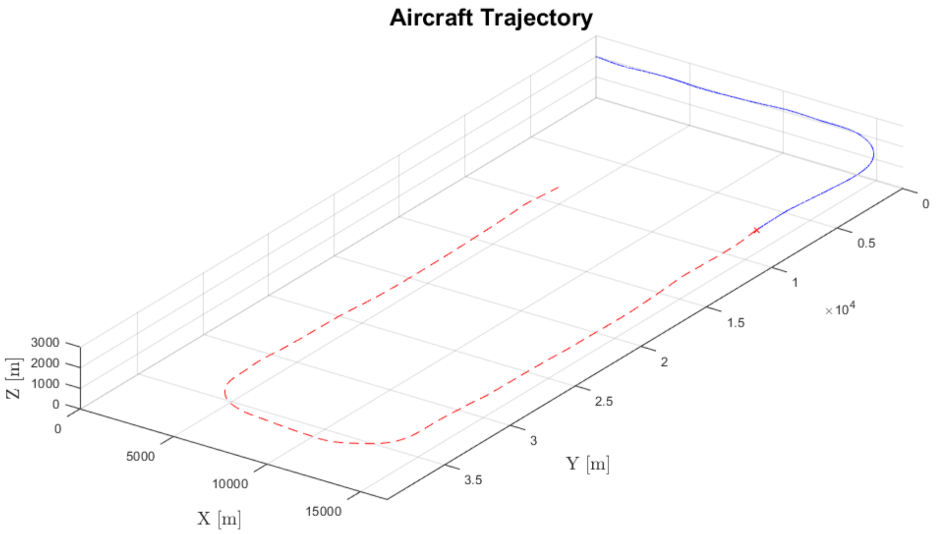

Figure 5.1: Aircraft Trajectory of Validation Flight with Failure using the Manual Classical Controller

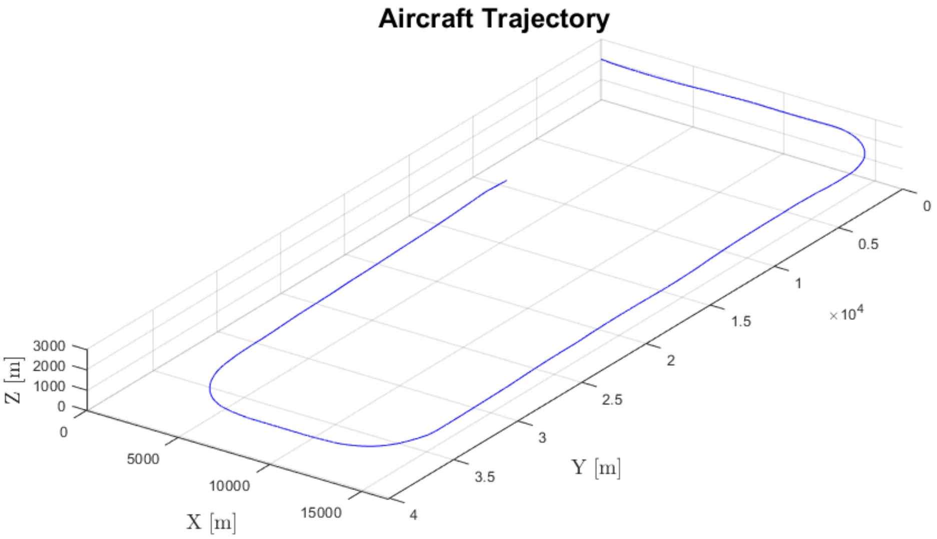

Figure 5.2: Aircraft Trajectory of Validation Flight without Failure using the Manual Classical Controller

5.2.2. Control Surface Deflections & Reference Command Inputs

The time histories of the control surface deflections along with the reference command inputs supplied by the joystick of the two validation flights, with and without failure, are shown in Figure 5.3 and Figure 5.4 respectively.

The classical rate controller aircraft has a fast response to the pilot's commands. The control surface deflections, specially in the yaw rate channel, closely track the reference command inputs.

The elevator surface is deflected for prolonged periods of time by the classical rate controller to counteract the pitching moment caused by the thrust of the engines. The classical rate controller also ensures that the aircraft remains steady during turns by counteracting the roll and pitch rate by deflecting the aileron and elevator surfaces. However, some pilot inputs are still required to keep the aircraft in the desired turn orientation.

The aileron hardover failure is clearly visible by the peak in the aileron deflection in Figure 5.3. The failure is quickly counteracted by the classical rate controller thanks to the roll rate feedback, aiding the pilot in not having to counteract the roll rate caused by the failure himself.

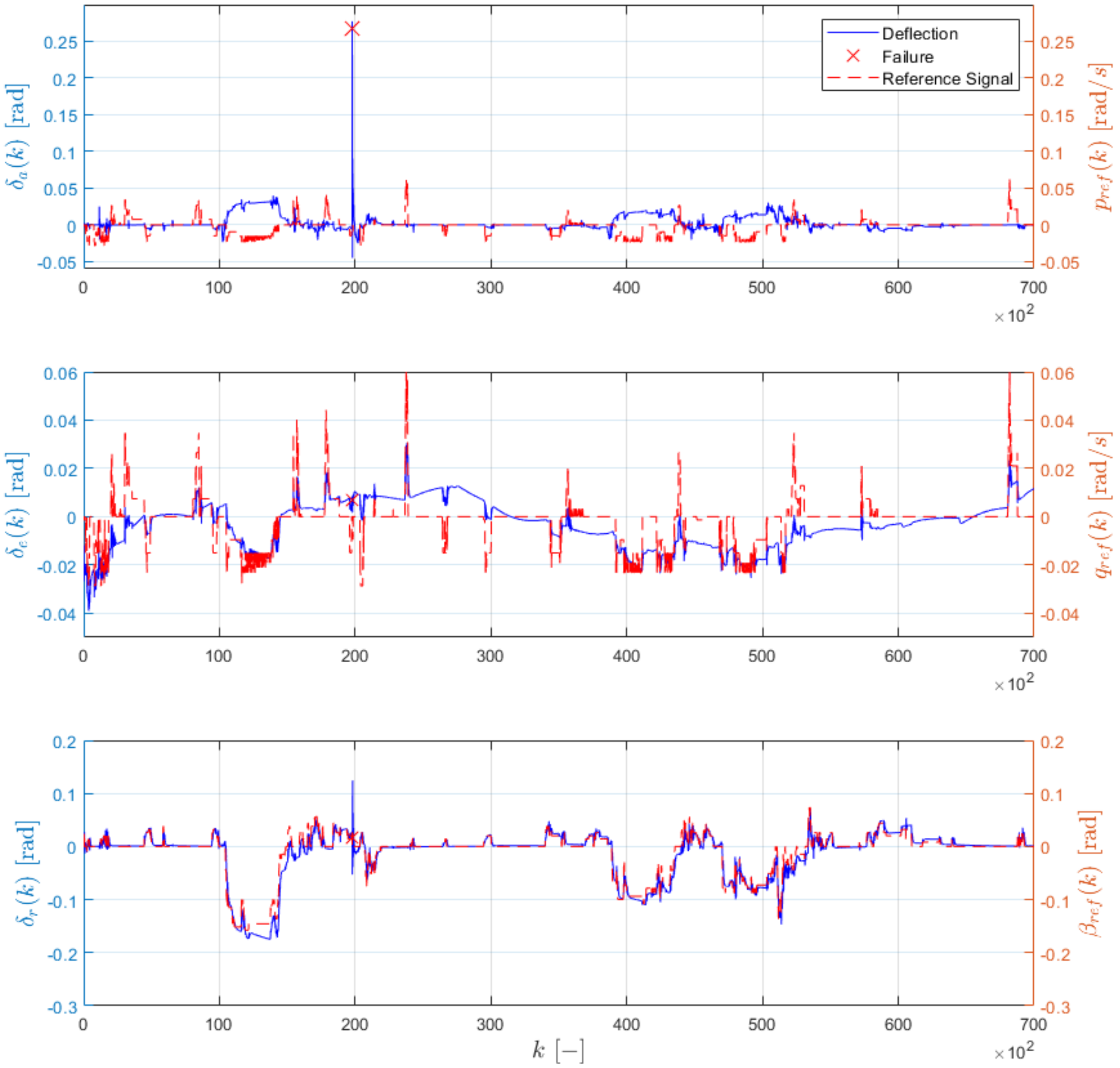

Figure 5.3: Control Surface Deflections & Reference Command Inputs of Validation Flight with Failure using the Manual Classical Rate Controller

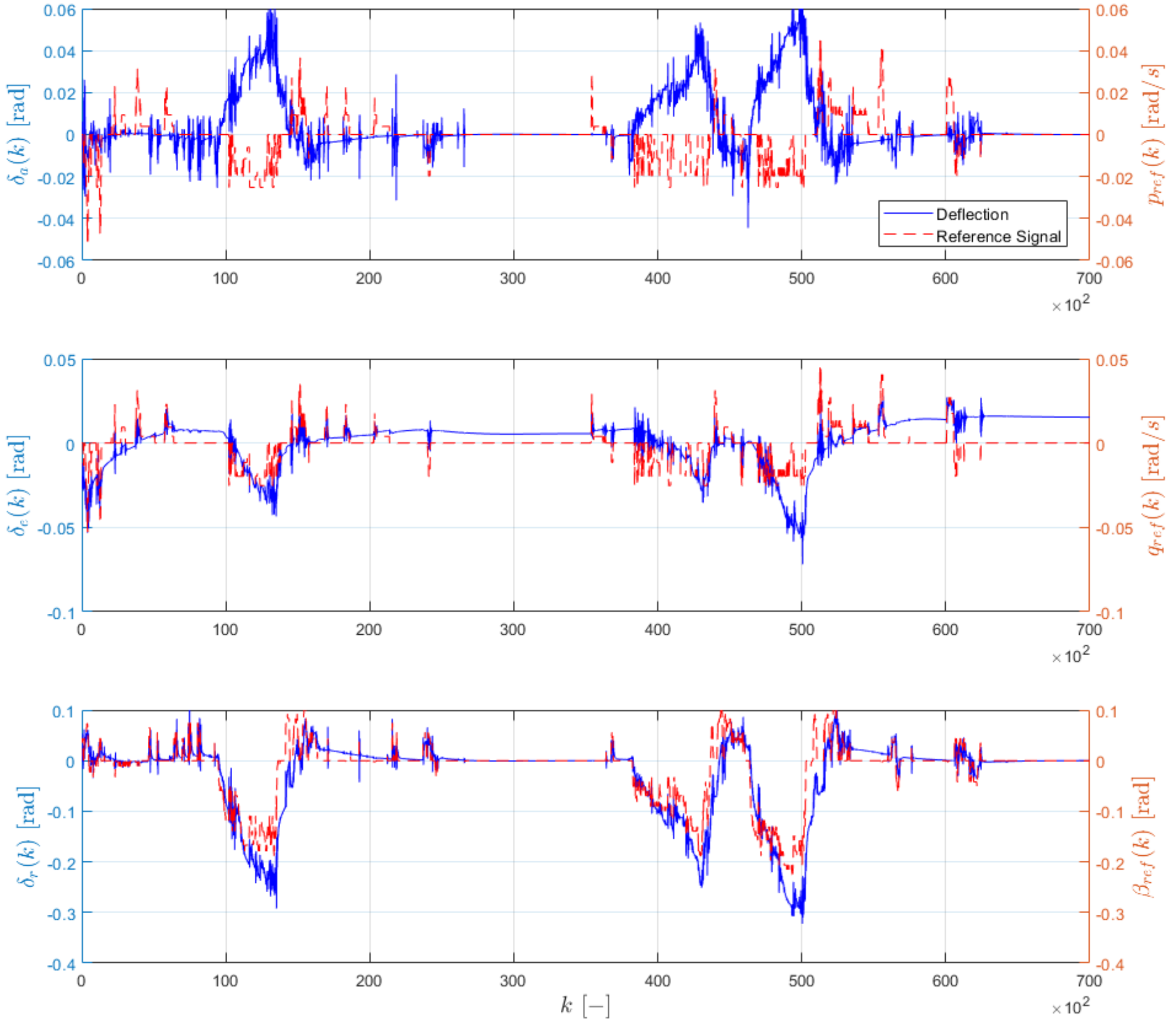

Figure 5.4: Control Surface Deflections & Reference Command Inputs of Validation Flight without Failure using the Manual Classical Rate Controller

6 ANDI Controller

A manual ANDI controller is designed for the cessna citation simulink model. An ANDI controller uses the estimated stability and control derivatives from the on-line aerodynamic model identification algorithm developed in chapter 4 in a Nonlinear Dynamic Inversion (NDI) controller. An NDI controller introduces a virtual input vector ν to then solve for the input u of the nonlinear system following the structure of Equation 6.1.

$$u = b^{-1}(x)[\nu - a(x)] \tag{6.1}$$

The design of the ANDI controller is outlined in section 6.1. The data of two validation flights, one with failure and one without, using the ANDI controller is shown and analyzed in section 6.2.

6.1. ANDI Controller Design

The control inputs from the pilot are the reference angular rates p_{ref}, q_{ref} and the sideslip angle β_{ref} as pure yaw rate as pilot input to the rudder is not practical. Thus, a two-loop ANDI controller based on the concept of time scale separation is designed. The aircraft dynamics are separated between slow and fast dynamics, into an outer and inner loop respectively, essentially applying NDI twice. The slow dynamics correspond to the kinematic equations of the sideslip control loop while the fast dynamics correspond to the the dynamic equations of the angular rates. The overall structure of the two-loop ANDI controller is shown in Figure 6.1.

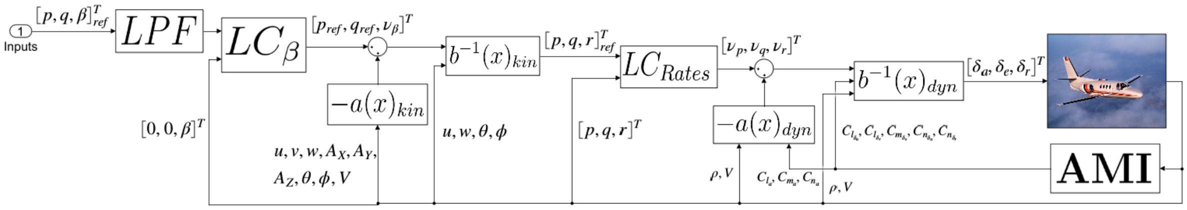

1
Inputs
$[p,q,\beta]^T_{ref}$
LPF
LC_β
$[p_{ref}, q_{ref}, \nu_\beta]^T$
$b^{-1}(x)_{kin}$
$-a(x)_{kin}$
$[p,q,r]^T_{ref}$
LC_{Rates}
$[\nu_p, \nu_q, \nu_r]^T$
$-a(x)_{dyn}$
$b^{-1}(x)_{dyn}$
$[\delta_a, \delta_e, \delta_r]^T$
$[0,0,\beta]^T$
$u, v, w, A_X, A_Y, A_Z, \theta, \phi, V$
u, w, θ, ϕ
$[p,q,r]^T$
ρ, V
$C_{l_a}, C_{m_a}, C_{n_a}$
$C_{l_{\delta_a}}, C_{l_{\delta_r}}, C_{m_{\delta_e}}, C_{n_{\delta_a}}, C_{n_{\delta_r}}$
ρ, V
AMI

Figure 6.1: Structure of two-loop ANDI Controller

The control inputs p_{ref}, q_{ref} & β_{ref} are first passed through the first order filters: $LPF_p = \frac{15}{s+15}$, $LPF_q = \frac{10}{s+10}$ & $LPF_\beta = \frac{0.5}{s+0.5}$ respectively to prevent brusque robot-like reactions of the ANDI controlled vehicle to the pilot inputs.

The sideslip angle β_{ref}, supplied by the twist handle of the joystick is passed through the linear controller shown in Equation 6.2 with $K_{P_1} = 1$ and $K_{I_1} = 0.5$ to obtain the virtual control angle ν_β used in the kinematic inversion.

$$\nu_\beta = \dot{\beta} = K_{P_1}\left(\beta_{ref} - \beta_{act}\right) + K_{I_1}\left(\beta_{ref} - \beta_{act}\right) + \frac{d}{dt}\beta_{ref} \tag{6.2}$$

Kinematic inversion is then performed using the virtual sideslip rate ν_β in Equation 6.3 following the structure of an NDI controller in Equation 6.1 to obtain the reference yaw rate r_{ref}.

$$\begin{bmatrix} p \\ q \\ r \end{bmatrix}_{ref} = \begin{bmatrix} 1 & 0 & 0 \\ 0 & 1 & 0 \\ \frac{w}{\sqrt{u^2+w^2}} & 0 & \frac{-u}{\sqrt{u^2+w^2}} \end{bmatrix}^{-1} \cdot \left(\begin{bmatrix} p_{ref} \\ q_{ref} \\ \nu_\beta \end{bmatrix} - \begin{bmatrix} 0 \\ 0 \\ \frac{1}{\sqrt{u^2+w^2}} \left[\frac{-uv}{V^2} a_x + (1 + \frac{v}{V^2}) a_y - \frac{vw}{V^2} a_z \right] \end{bmatrix} \right) \tag{6.3}$$

$$
\begin{aligned}
&\text{Where :}\\
&\quad a_x = (A_x - g\sin(\theta))\\
&\quad a_y = (A_y + g\sin(\phi)\cos(\theta))\\
&\quad a_z = (A_z + g\cos(\phi)\cos(\theta))\\
&\text{and}\\
&\quad u = V\cdot\cos(\alpha)\cdot\cos(\beta)\\
&\quad v = V\cdot\cos(\beta)\\
&\quad w = V\cdot\sin(\alpha)
\end{aligned}
$$

The outputs of the kinematic inversion, the reference angular rates, are then passed through the linear controller shown in Equation 6.4 with $K_{P_2} = 8$ and $K_{I_2} = 2$ to obtain the virtual angular accelerations $\nu_{p,q,r}$ used in the dynamic inversion.

$$
\begin{bmatrix} \nu_p \\ \nu_q \\ \nu_r \end{bmatrix} = K_{P_2}\left(\begin{bmatrix} p \\ q \\ r \end{bmatrix}_{\text{ref}} - \begin{bmatrix} p \\ q \\ r \end{bmatrix}_{\text{act}}\right) + K_{I_2}\int\left(\begin{bmatrix} p \\ q \\ r \end{bmatrix}_{\text{ref}} - \begin{bmatrix} p \\ q \\ r \end{bmatrix}_{\text{act}}\right)\int dt + \frac{d}{dt}\begin{bmatrix} p \\ q \\ r \end{bmatrix}_{\text{ref}} \tag{6.4}
$$

Dynamic inversion is then performed, following the structure of an NDI in Equation 6.1, using the virtual angular accelerations vector $\nu_{p,q,r}$ in Equation 6.5 to obtain the control surface deflections. The stability and control derivatives used in the dynamic inversion are supplied by the estimates of the on-line AMI algorithm.

$$
\begin{aligned}
\begin{bmatrix} \delta_a \\ \delta_e \\ \delta_r \end{bmatrix} = \begin{bmatrix} bC_{l_{\delta_a}} & 0 & bC_{l_{\delta_r}} \\ 0 & \bar{c}C_{m_{\delta_e}} & 0 \\ bC_{n_{\delta_a}} & 0 & bC_{n_{\delta_r}} \end{bmatrix}^{-1} \cdot \frac{I}{\frac{1}{2}\rho V^2 S} \cdot \left\{ \begin{bmatrix} \nu_p \\ \nu_q \\ \nu_r \end{bmatrix} + \right. \\
\left. I^{-1}\left(\begin{bmatrix} p \\ q \\ r \end{bmatrix} \times I \begin{bmatrix} p \\ q \\ r \end{bmatrix} - \frac{1}{2}\rho V^2 S \begin{bmatrix} bC_{l_a} \\ \bar{c}C_{m_a} \\ bC_{n_a} \end{bmatrix}\right)\right\}
\end{aligned} \tag{6.5}
$$

$$
\begin{aligned}
&\text{Where :}\\
&\quad I = \begin{bmatrix} I_{xx} & 0 & -I_{xz} \\ 0 & I_{yy} & 0 \\ -I_{xz} & 0 & I_{zz} \end{bmatrix}\\
&\text{and}\\
&\begin{bmatrix} C_{l_a} \\ C_{m_a} \\ C_{n_a} \end{bmatrix} = \begin{bmatrix} C_{l_0} + \beta C_{l_\beta} + \frac{pb}{2V} C_{l_p} + \frac{rb}{2V} C_{l_r} \\ C_{m_0} + \alpha C_{m_\alpha} + \frac{qc}{V} C_{m_q} \\ C_{n_0} + \beta C_{n_\beta} + \frac{pb}{2V} C_{n_p} + \frac{rb}{2V} C_{n_r} \end{bmatrix}
\end{aligned}
$$

6.2. Validation Flights

The ANDI controller developed in section 6.1 has been used to fly the Cessna Citation simulink model in two validation flights, one with failure and one without. The data of the validation flights is shown and analysed in this section. The aircraft trajectories of the two validation flights are included in subsection 6.2.1. The time histories of the control surface deflections along with the reference command inputs supplied by the joystick are shown and analyzed in subsection 6.2.2. The time histories of the moving squared average metric used in the monitoring algorithm are shown in subsection 6.2.3. Finally, the time histories showing the convergence of the asymmetric stability and control derivative estimates for the ANDI controller with and without failure are shown and analyzed in subsection 6.2.4, the symmetric stability and control derivative estimate are shown in Appendix A. The performance of the ANDI controller compared to the classical rate controller is qualitatively analyzed in subsection 6.2.5.

6.2.1. Aircraft Trajectories

The aircraft trajectories of the validation flights with and without failure are shown in Figure 6.2 and Figure 6.3 respectively.

The turns of both validation flights are slightly tighter than those of the validation trajectory example provided. Furthermore, the turns performed in the validation flight with failure are more gentle than those of the validation flight without failure as the pilot is more cautious when performing the turns after the failure. The validation flight with failure is also wider and thus longer than the validation without failure.

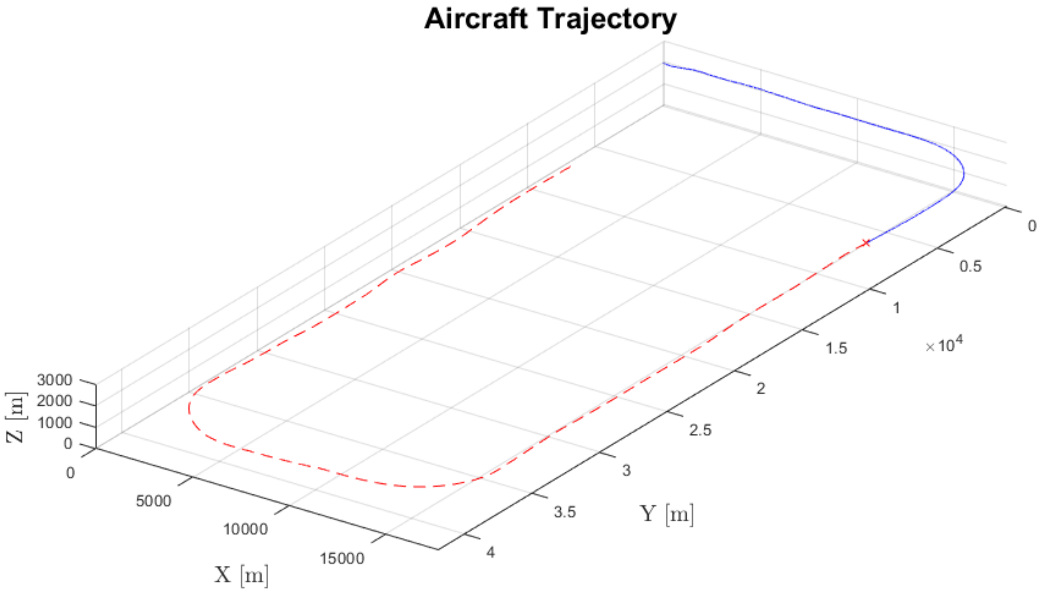

Figure 6.2: Aircraft Trajectory of Validation Flight with Failure using the Manual ANDI Controller

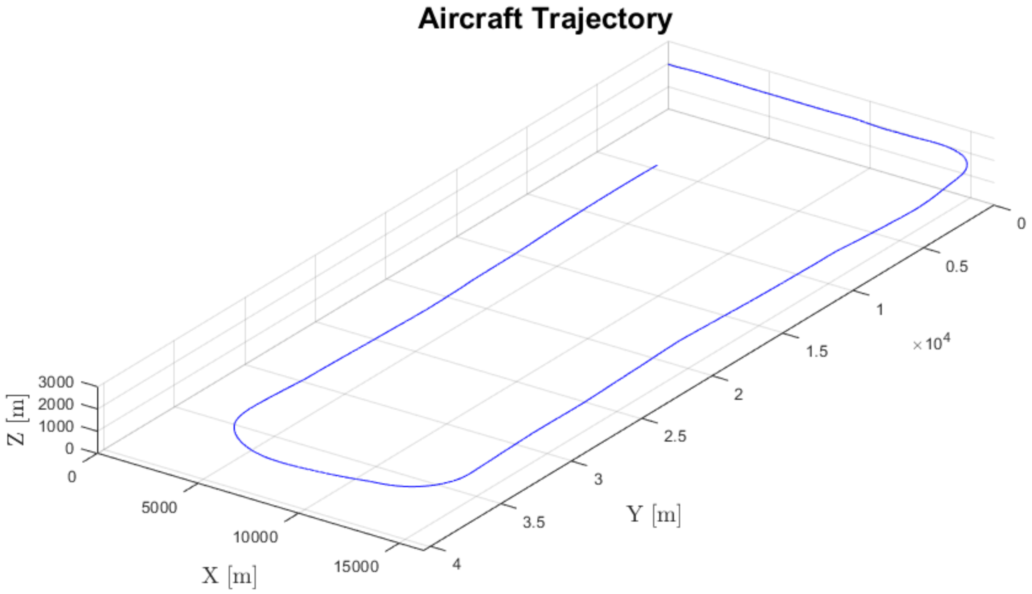

Figure 6.3: Aircraft Trajectory of Validation Flight without Failure using the Manual ANDI Controller

6.2.2. Control Surface Deflections & Reference Command Inputs

The time histories of the control surface deflections along with the reference command inputs supplied by the joystick of the two validation flights with and without failure are shown in Figure 6.4 and Figure 6.5 respectively.

The ANDI controlled aircraft is sluggish to respond to pilot input's in comparison to the classical rate controller. Furthermore, the ANDI controller causes oscillations in the control surface deflections which indicates that it is underdamped resulting in an unpleasant flying experience and increased wear of the control surface actuators.

The ANDI controller, thanks to the sideslip controller, deflects the aileron and elevator surfaces in order to keep the aircraft in the desired sideslip angle during turns. Very few pilot inputs are required during turns to keep the aircraft in the desired orientation thus making turns more seamless for pilots in comparison to the classical rate controller.

The aileron hardover failure is clearly visible by the peak in the aileron deflection δ_a in Figure 6.4. The failure is quickly counteracted by the ANDI controller which uses the estimates of the stability and control derivatives of the failed aircraft quickly determined thanks to the reset of the asymmetric coefficients covariance matrix triggered by the AMI monitoring algorithm.

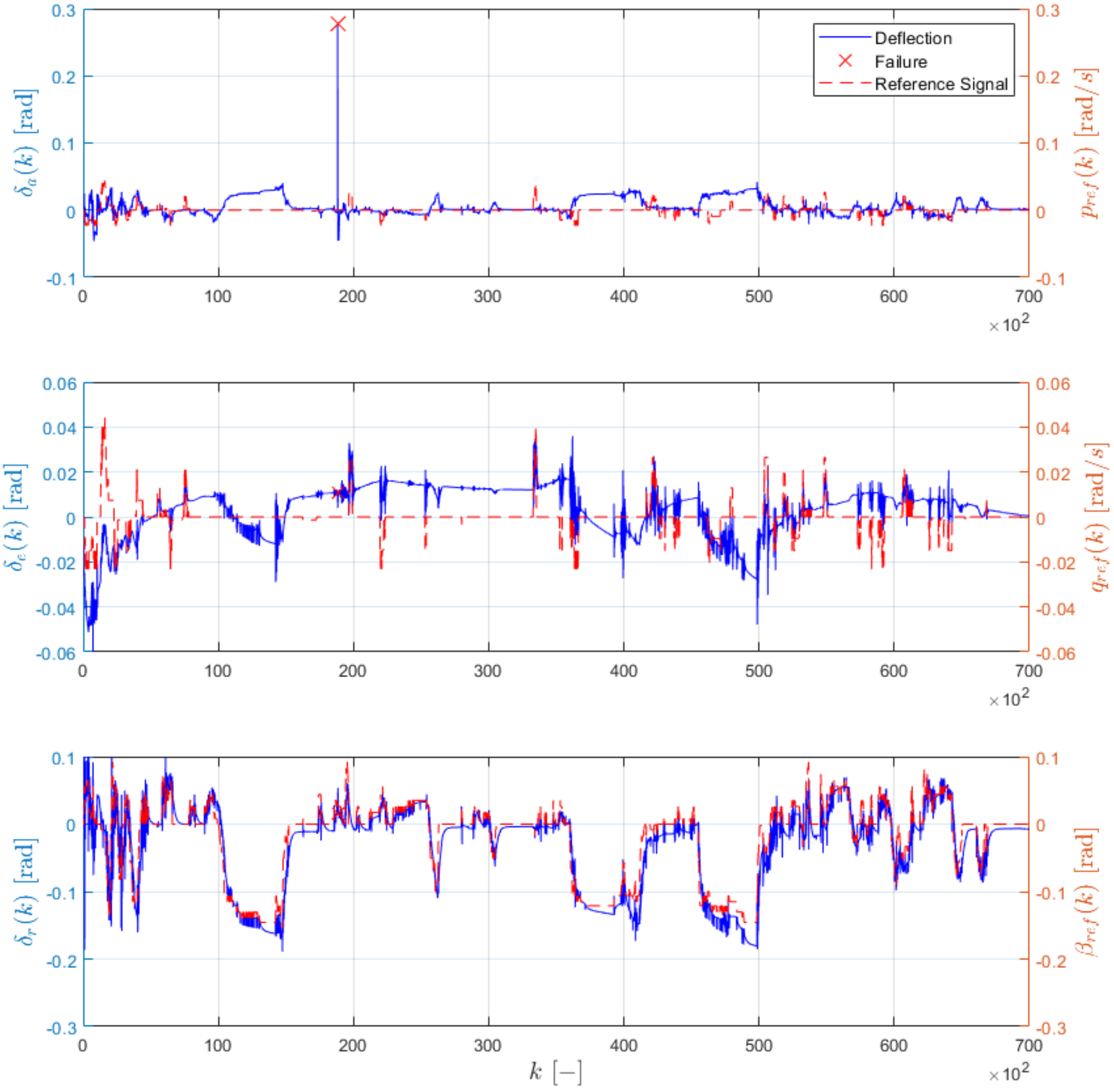

Figure 6.4: Control Surface Deflections & Reference Command Inputs of Validation Flight with Failure using the Manual ANDI Controller

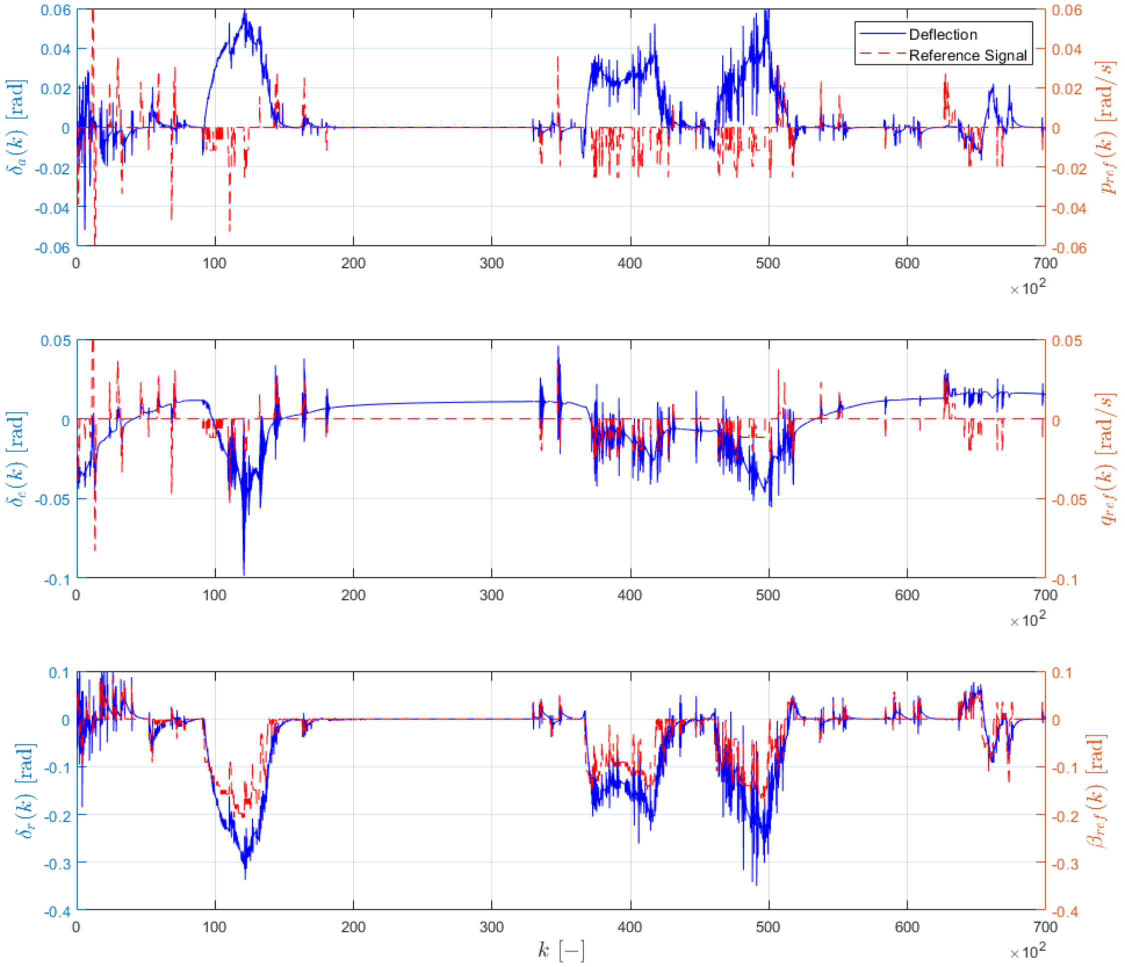

Figure 6.5: Control Surface Deflections & Reference Command Inputs of Validation Flight without Failure using the Manual ANDI Controller

6.2.3. Statistical Monitoring Metric

The time histories of the moving squared average metric used as the AMI monitoring algorithm of the validation flights with and without failure are shown in Figure 6.6.

The peak of the C_l moving squared average innovation caused by the failure decreased by a factor of 10 in comparison to the values in subsection 4.1.1 due to the ANDI controller. To ensure that the monitoring algorithm detects the failure and discards possible false positives the threshold values are determined again with the ANDI controller, shown in Table 6.1. With the new threshold values the AMI monitoring algorithm performed well at detecting the aileron hardover failure and discarding any false positives, resetting the asymmetric coefficients covariance matrix after the failure allowing for the quick estimation of the changed stability and control derivative values.

Table 6.1: Moving Squared Average Mean, Failure and Threshold Values using the Manual ANDI Controller

Coefficients	$\overline{\Delta}(\mathbf{k})_{\mathbf{max}}$ [−]	$\overline{\Delta}(\mathbf{k})_{\mathbf{fail}}$ [−]	$\overline{\Delta}(\mathbf{k})_{\mathbf{thr}}$ [−]
$\mathbf{C_X}$	$8.67 \cdot 10^{-4}$	-	0.053
$\mathbf{C_Y}$	$1.90 \cdot 10^{-5}$	-	$1.15 \cdot 10^{-3}$
$\mathbf{C_m}$	$7.70 \cdot 10^{-4}$	-	0.047
$\mathbf{C_Y}$	$5.45 \cdot 10^{-5}$	$7.69 \cdot 10^{-5}$	$3.31 \cdot 10^{-3}$
$\mathbf{C_l}$	$8.91 \cdot 10^{-7}$	$1.08 \cdot 10^{-4}$	$5.41 \cdot 10^{-5}$
$\mathbf{C_n}$	$8.47 \cdot 10^{-6}$	$8.47 \cdot 10^{-6}$	$5.14 \cdot 10^{-4}$

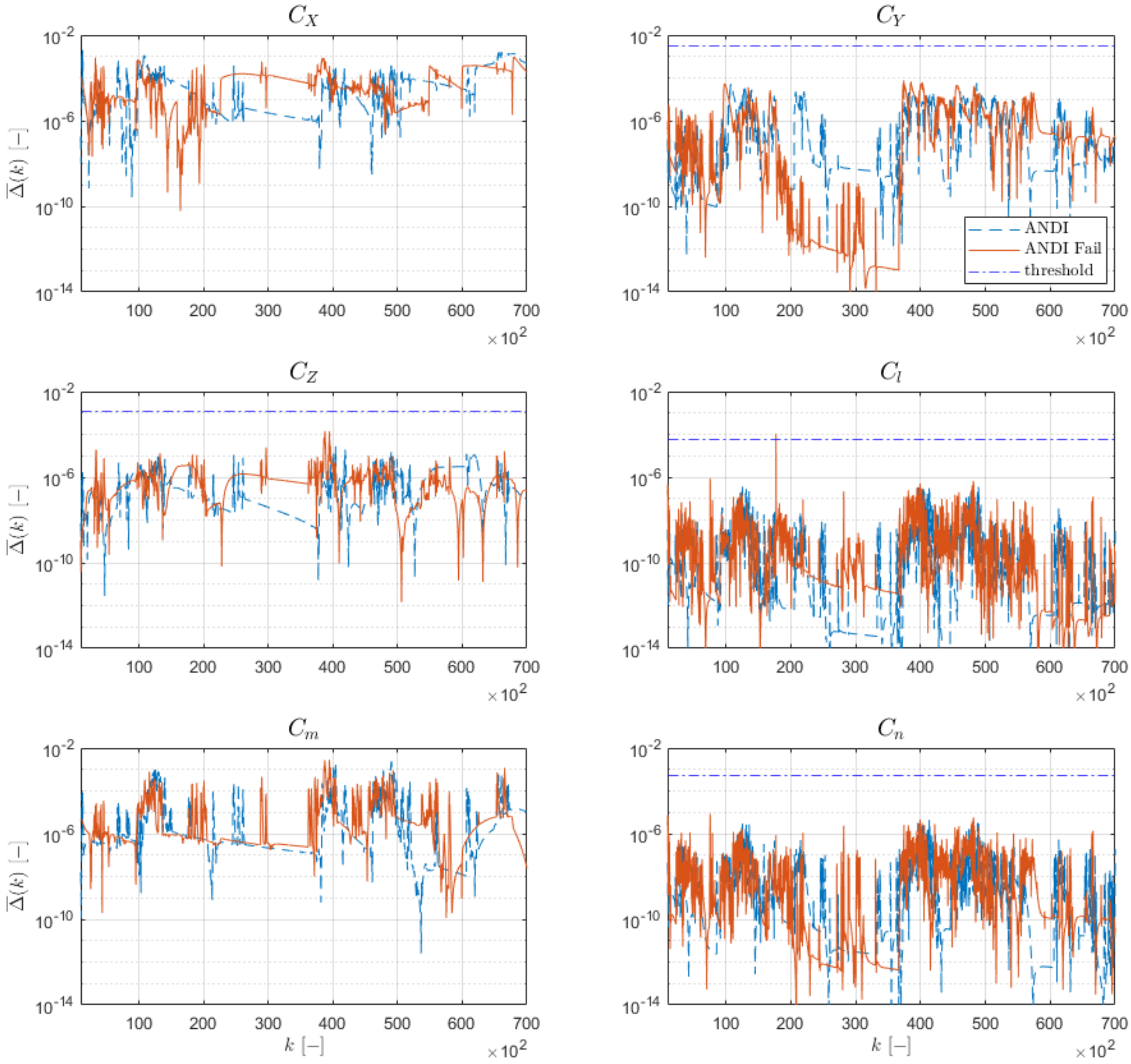

Figure 6.6: Average Squared Innovation Metric of Validation Flights using the Manual ANDI Controller

6.2.4. Stability & Control Derivative Estimates

The time histories showing the convergence of the asymmetric stability and control derivative estimates of the validation flights with and without failure are shown in Figure 6.7, Figure 6.8 and Figure 6.9. The symmetric stability and control derivative estimates are included in Appendix A.

The on-line aerodynamic model identification algorithm performs well at estimating the stability and control derivatives before and after the failure. The AMI algorithm quickly converges towards the parameter estimates starting from an initial guess. The stability and control derivative estimates throughout all force and moment coefficients before the failure are approximately the same for both validation flights, which indicates a reliable convergence of the estimates towards the stability and control derivative values.

The failure caused a notable negative change in the C_{Y_0} estimate, as predicted in subsection 2.2.1. The drag produced by both wings will have a lateral component acting in opposite directions due to the wing sweep, however the drag of the right wing which has the downward deflection aileron is greater than the drag of left wing which results in a net negative lateral force. The estimate of $C_{Y_{\delta_a}}$ was predicted to be halved, however the decrease was much less significant perhaps due to the relationship between aileron deflection and lateral force not being linear. The effect of the failure on the other estimates was less severe, most of them converging to approximately the same value as the estimates of the validation flight without failure with the exception of the C_{Y_p} estimate. The estimate of C_{Y_p} was lower for the failed aircraft indicating that having the aileron deflected results in a lower lateral force with roll rate.

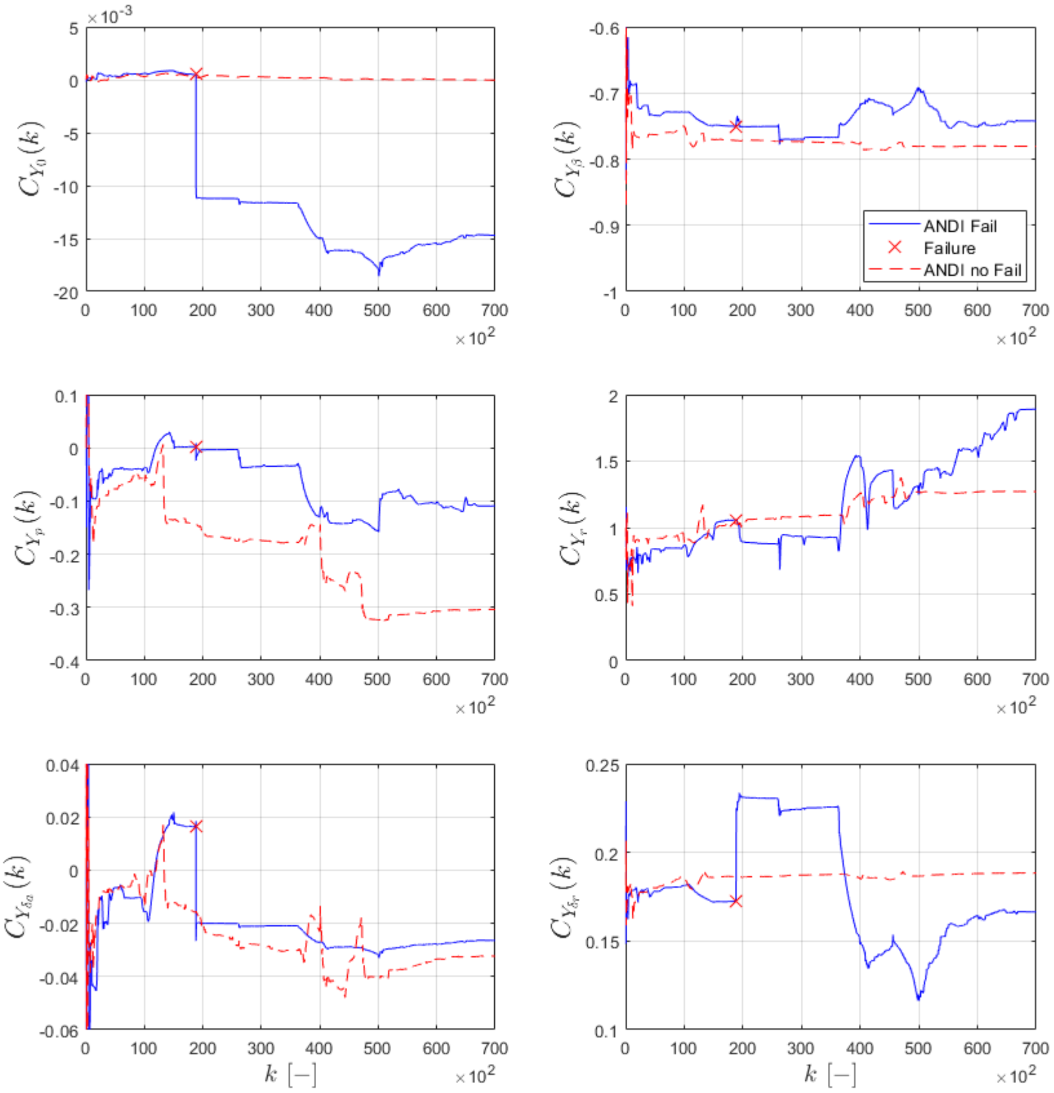

Figure 6.7: C_Y Stability and Control Derivative Estimates of Validation Flights using the Manual ANDI Controller

The failure has a significant effect on the C_{l_0}, $C_{l_{\delta_a}}$ & C_{l_p} estimates. The negative change in the C_{l_0} estimate is caused by the right wing with the downward deflecting aileron having more lift than the left wing producing a constant anti-clockwise rolling moment. As expected, the value of the $C_{l_{\delta_a}}$ estimate is approximately halved as a result of the aileron effectiveness being halves as effectively only one aileron is operational. The C_{l_p} estimate increased after the failure indicating that having the aileron deflected increases the opposing rolling moment with roll rate. After the failure, the estimates of the other C_l stability and control derivatives converge to approximately the same values as the estimates of the un-failed aircraft thus have not been significantly affected by the aileron hardover failure.

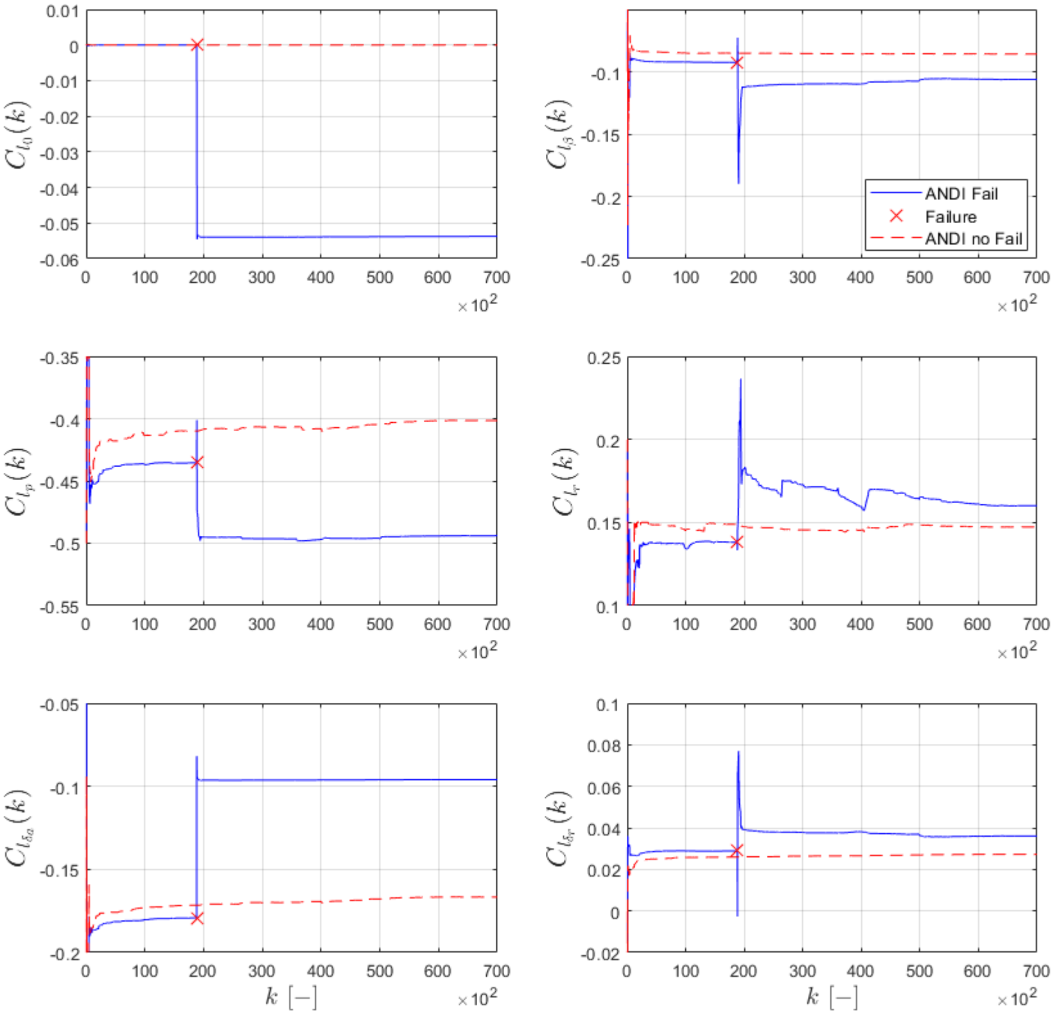

Figure 6.8: C_l Stability and Control Derivative Estimates of Validation Flights using the Manual ANDI Controller

The effect of the failure on the C_n stability and control derivative estimates follows a similar pattern, where the C_{n_0}, $C_{n_{\delta_a}}$ & C_{n_p} estimates are the most affected. As predicted in subsection 2.2.1, the failure causes a negative change in the C_{n_0} estimate due to the drag of the right wing with the downward deflecting aileron being greater than the drag of the left wing producing a constant anti-clockwise yawing moment. Similarly, the yawing moment produced by the drag difference when deflecting the ailerons is also halved as effectively only one aileron is operational, thus halving the value of the $C_{l_{\delta_a}}$ estimate. Finally the value of the C_{l_p} estimates is lower for the failed aircraft which indicates that having the aileron deflected with a roll rate produces a lower yawing moment. The values of the other C_n stability and control derivatives converge to approximately the same estimates as those of the un-failed aircraft.

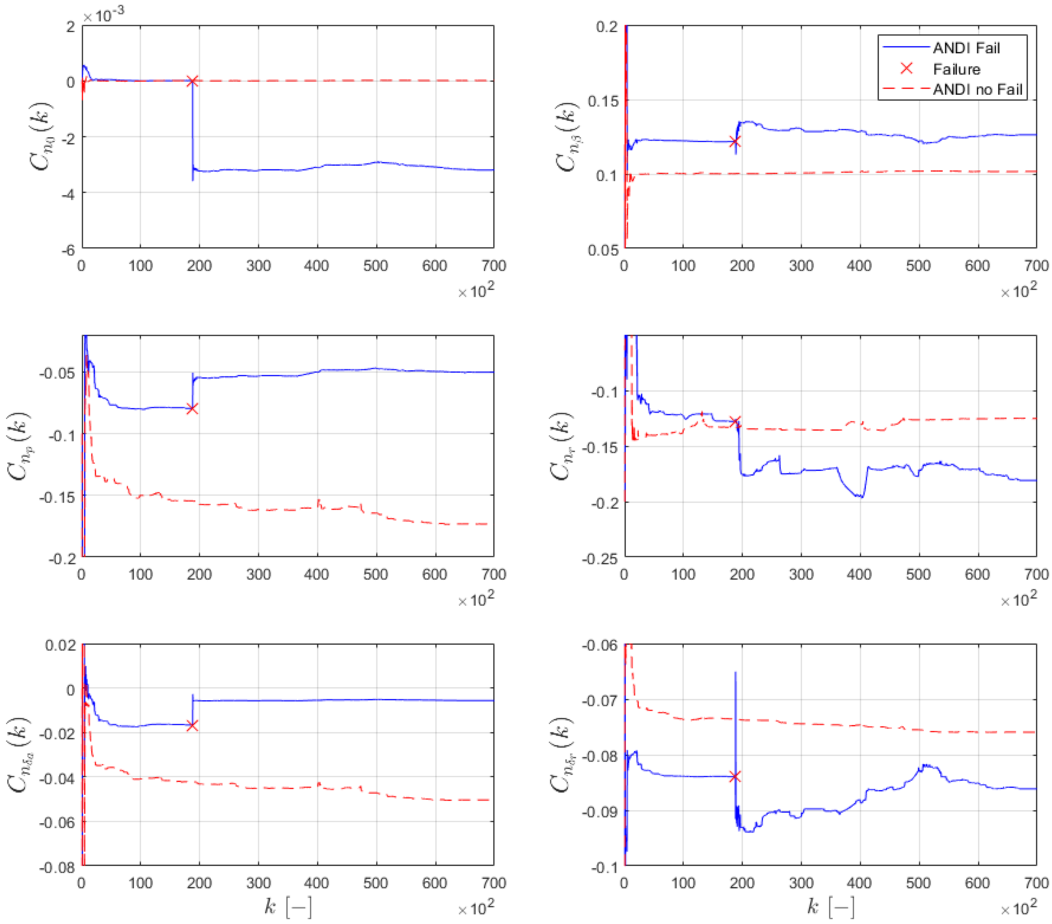

Figure 6.9: C_n Stability and Control Derivative Estimates of Validation Flights using the Manual ANDI Controller

6.2.5. Comparison with Classical Rate Controller

The ANDI and classical rate controller both successfully completed the validation flights. The ANDI controlled aircraft was slightly more sluggish to respond to the pilot inputs, however the turns performed with the ANDI controller are more seamless as barely no reference pitch or roll rate input is required from the pilot to keep the aircraft steady.

The ANDI controller performs well when the aircraft's aerodynamics can be accurately modeled by the AMI algorithm, such as in the validation flights. However if the aircraft's aerodynamics are highly nonlinear, such as in stall or extreme control surface deflections, the AMI algorithm struggles to accurately model the aircraft's aerodynamics which leads to brusque behaviour of the ANDI controller. A more complex aerodynamic model or placing limits on the stability and control derivative estimates could be implemented to make the ANDI controller more versatile to extreme situations. In comparison, the classical rate controller does not rely on AMI algorithm estimates and thus can be tuned to be significantly more responsive to pilot inputs without resulting in brusque behaviour of the controller.

Both controllers counteract the aileron deflection caused by the failure, aiding the pilot in not having to counteract roll rate of the failure himself. The main difference between both controllers is the effectiveness of the roll rate channel, it's halved for the classical rate controller as effectively only one aileron is operational. There is no change in the effectiveness of the roll rate channel for the ANDI controller as the halving of the aileron effectiveness is accounted for by the $C_{l_{\delta_a}}$ estimate obtained from the AMI algorithm, doubling the aileron deflection to compensate. While the ANDI controller diminishes the effect of the failure on the roll rate channel it also removes an important motion queue for the pilots to determine the failure type, it is essential that the pilots are aware of the effect of the failure on the aircraft's flying characteristics. A lack of knowledge could lead to catastrophic consequences, for example when performing a left turn after the failure both controllers will attempt to compensate for the rolling moment of the aircraft by deflecting the aileron however they may reach the aileron deflection limit causing the aircraft to unexpectedly roll leftwards.

7
INDI Controller

A manual INDI controller computes the changes of the control surface deflections with respect to their current deflections rather than computing the complete control surface deflections in the ANDI controller. There are two advantages of using an INDI controller over an ANDI controller, it has a lower reliance on the estimates of the AMI algorithm reducing the impact of model mismatch, the other advantage is that it is not affected if the control derivatives are nonlinear. The INDI controller can be derived from the general nonlinear system in Equation 7.1.

$$\underline{\dot{x}} = \underline{f}\left(\underline{x}, \underline{u}\right) \tag{7.1}$$

Performing the first order Taylor series expansion of Equation 7.1, the general nonlinear system is linearized in Equation 7.2 at the current time point.

$$\underline{\dot{x}} = \underline{\dot{x}}_0 + F\left(\underline{x}_0, \underline{u}_0\right)\left(\underline{x} - \underline{x}_0\right) + G\left(\underline{x}_0, \underline{u}_0\right)\left(\underline{u} - \underline{u}_0\right) \tag{7.2}$$

Given that the sample rate is considered to be high Equation 7.2 can be further simplified into Equation 7.3 using the time scale separation principle.

$$\underline{\dot{x}} \simeq \underline{\dot{x}}_0 + G\left(\underline{x}_0, \underline{u}_0\right)\Delta\underline{u} \tag{7.3}$$

An NDI controller is then designed in an incremental form in Equation 7.4, where $\underline{\dot{x}}_0$ is measured and $G\left(\underline{x}_0, \underline{u}_0\right)$ is the control effectiveness matrix.

$$\Delta\underline{u} = G^{-1}\left(\underline{x}_0, \underline{u}_0\right)\left(\underline{\nu} - \underline{\dot{x}}_0\right) \tag{7.4}$$

The design of the INDI controller is outlined in section 7.1. The data of two validation flights, one with failure and one without, using the INDI controller is shown and analyzed in section 7.2.

7.1. INDI Controller Design

The control inputs of the INDI controller are the same as those of the ANDI controller, the reference angular rates p_{ref}, q_{ref} and sideslip angle β_{ref}. A two-loop INDI controller based on the principle of time scale separation is designed, where the outer sideslip control loop is identical to that of the ANDI controller but the inner dynamic loop is an INDI controller. The overall structure of the two-loop INDI controller is shown in Figure 7.1

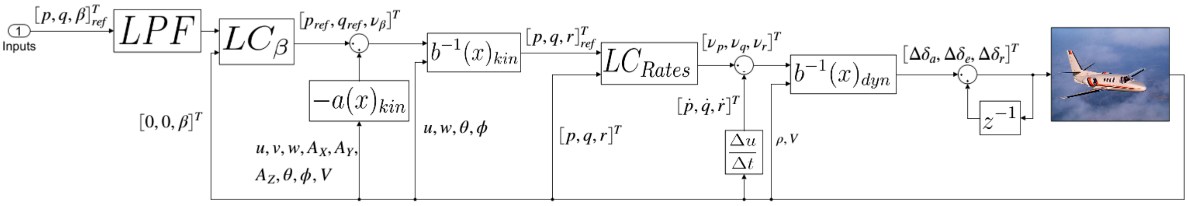

Figure 7.1: Structure of two-loop INDI Controller

The control inputs are first passed through the low pass filters: $LPF_p = \frac{15}{s+15}$, $LPF_q = \frac{15}{s+15}$ & $LPF_\beta = \frac{0.6}{s+0.6}$ respectively such that the pilot inputs lead to smooth reactions of the INDI controlled aircraft. The reference sideslip angle β_{ref} is then passed through the linear controller shown in Equation 6.2 with $K_{P_1} = 1$ and $K_{I_1} = 0.5$ to obtain the virtual control angle ν_β used in the kinematic inversion. Kinematic inversion is then performed using the NDI controller in Equation 6.3 to obtain the reference yaw rate r_{ref}. The reference angular rates are then passed through the linear controller shown in Equation 6.4 with $K_{P_2} = 6$ and $K_{I_2} = 0.1$ to obtain the virtual acceleration vector $v_{p,q,r}$ used in the dynamic inversion.

Dynamic inversion is then performed, following the structure of an INDI controller in Equation 7.4, using the virtual angular acceleration vector $v_{p,q,r}$ and the derivatives of the measured angular rates in Equation 7.5 to obtain the changes of the control surface deflection with respect to their current positions. The control derivatives used in the dynamic inversion are $C_{l_{\delta_a}} = -0.184$, $C_{l_{\delta_r}} = 0.034$, $C_{m_{\delta_e}} = -0.894$, $C_{n_{\delta_a}} = -0.011$, $C_{n_{\delta_r}} = -0.097$, the average estimates of the AMI algorithm from Table 3.1.

$$\begin{bmatrix} \Delta\delta_a \\ \Delta\delta_e \\ \Delta\delta_r \end{bmatrix} = \begin{bmatrix} bC_{l_{\delta_a}} & 0 & bC_{l_{\delta_r}} \\ 0 & \bar{c}C_{m_{\delta_e}} & 0 \\ bC_{m_{\delta_a}} & 0 & bC_{m_{\delta_r}} \end{bmatrix}^{-1} \frac{I}{\frac{1}{2}\rho V^2 S} \left\{ \begin{bmatrix} v_p \\ v_q \\ v_r \end{bmatrix} - \begin{bmatrix} \dot{p} \\ \dot{q} \\ \dot{r} \end{bmatrix} \right\} \tag{7.5}$$

The response of the INDI controlled aircraft is extremely jittery to the pilot's inputs perhaps due to the influence of actuator dynamics. The computed changes of the control surface deflections in Equation 7.5 are reduced by a factor of 10 to smoothen the response of the aircraft.

The control surface deflections are obtained by recursively adding the changes of the control surface deflections with respect to their current positions computed in the dynamic inversion as shown in Equation 7.6.

$$\begin{bmatrix} \delta_a \\ \delta_e \\ \delta_r \end{bmatrix}_{i+1} = \begin{bmatrix} \delta_a \\ \delta_e \\ \delta_r \end{bmatrix}_{i} + \begin{bmatrix} \Delta\delta_a \\ \Delta\delta_e \\ \Delta\delta_r \end{bmatrix} \tag{7.6}$$

7.2. Validation Flights

The Cessna Citation simulink model is flown with the INDI controller developed in section 7.1 in two validation flights, one with failure and one without. The data of the validation flights is shown and analyzed in this section. The aircraft trajectories of the validation flights are shown in subsection 7.2.1. The time histories of the control surface deflections along with the reference command inputs are shown and analyzed in subsection 7.2.2. The performance of the INDI controller compared to the ANDI and classical rate controller is qualitatively analyzed in subsection 7.2.3.

7.2.1. Aircraft Trajectories

The aircraft trajectories of the two validation flights with failure and without failure are shown in Figure 7.2 and Figure 7.3 respectively.

The aircraft trajectories of both validation flights closely follow the validation trajectory example provided, however the turns are slightly tighter. There are no significant differences between the aircraft trajectories.

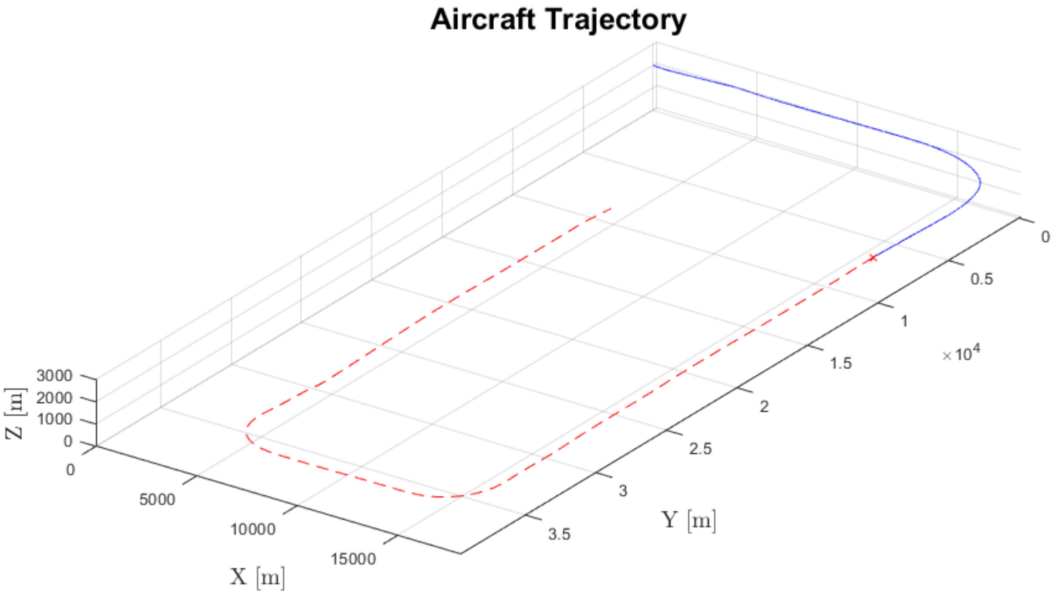

Figure 7.2: Aircraft Trajectory of Validation Flight with Failure using the INDI Controller

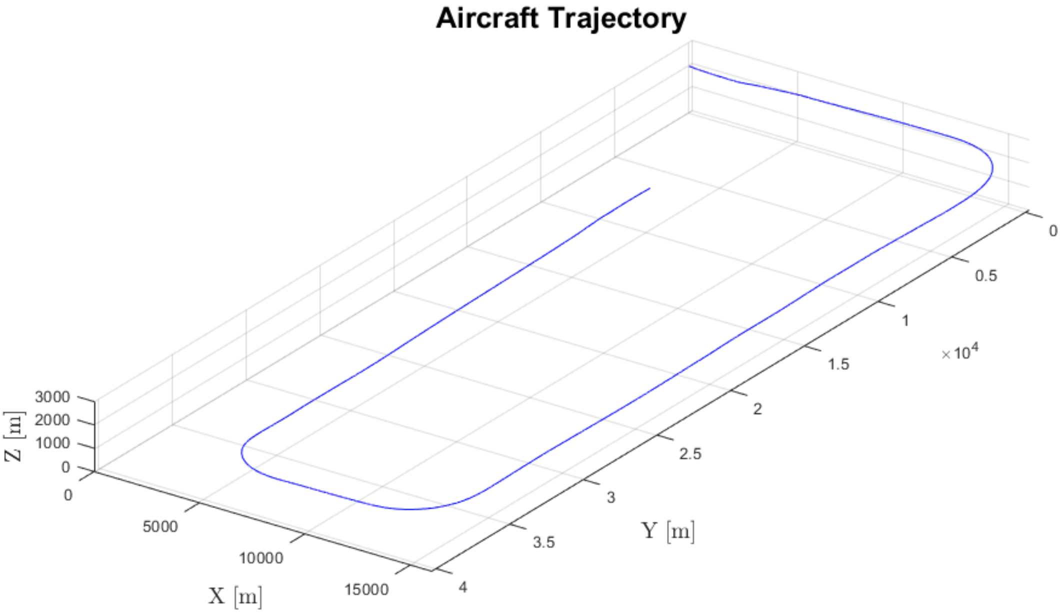

Figure 7.3: Aircraft Trajectory of Validation Flight without Failure using the INDI Controller

7.2.2. Control Surface Deflections & Reference Command Inputs

The time histories of the control surface deflections along with the reference command inputs supplied by the joystick of the two validation flights, with and without failure, are shown in Figure 7.4 and Figure 7.5 respectively.

The INDI controlled aircraft has a fast response to the pilot's commands, faster than the ANDI controller but slower than the classical rate controller. The changes in the control surface deflections are also significantly smoother than in the ANDI controller resulting in smoother reactions of the aircraft to the pilot's inputs. The INDI controlled aircraft requires the least pilot inputs, thus also the lowest pilot effort, out of all of the analyzed controllers to perform the validation flight.

The aileron hardover failure causes the same peak in the aileron deflection in Figure 7.4 as in the other controllers. The roll rate produced by the failure is quickly counteracted by the INDI controller, aiding the pilot in not having to constantly counteract the roll rate caused by the failure himself.

The sideslip controller performs best with the INDI controller, virtually no pitch or roll rate inputs are required from the pilot to keep the aircraft in the desired orientation during turns. The sideslip controller gains prove adequate for both executing turns and small sideslip corrections.

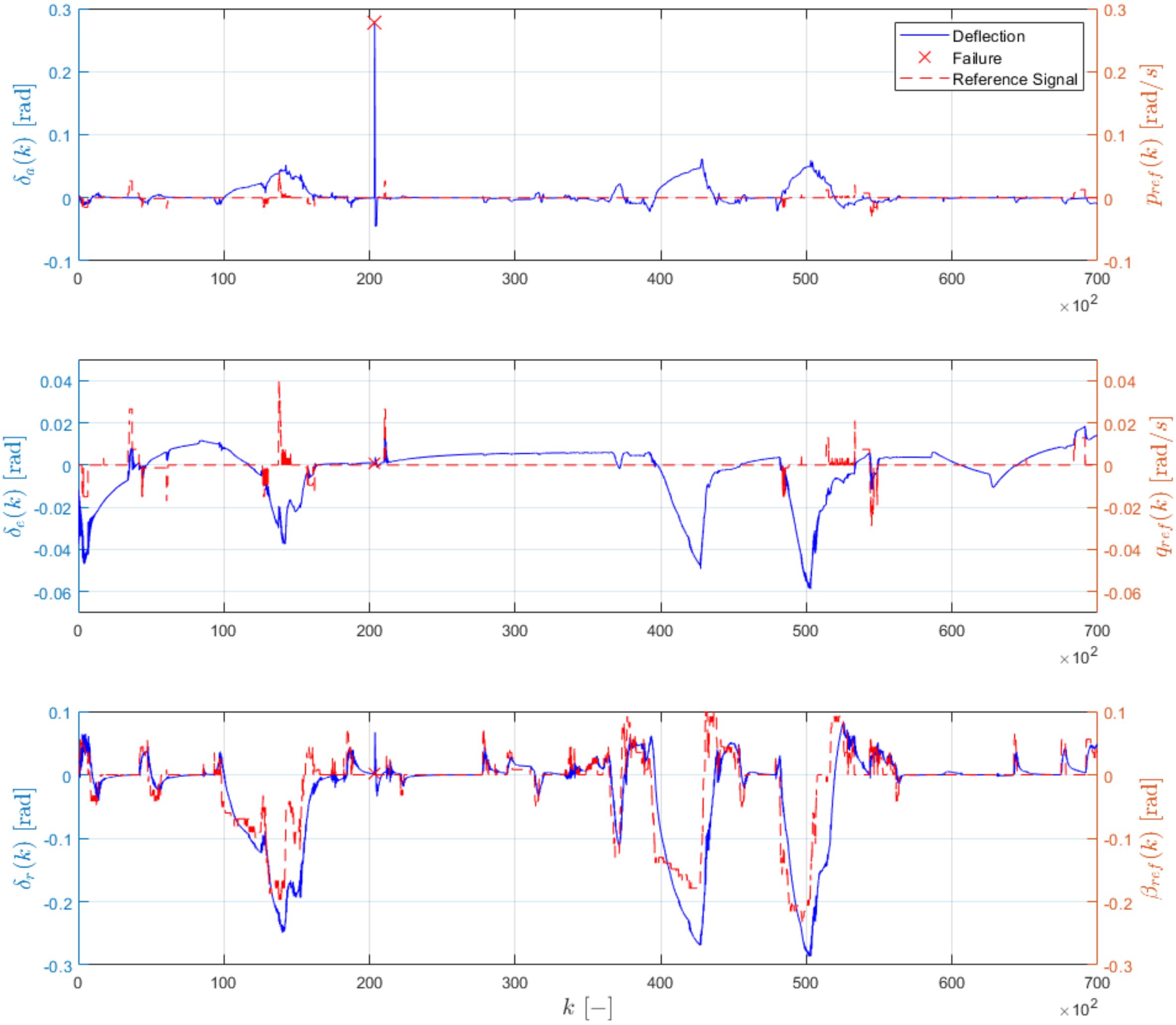

Figure 7.4: Control Surface Deflections & Reference Command Inputs of Validation Flight with Failure using the Manual INDI Controller

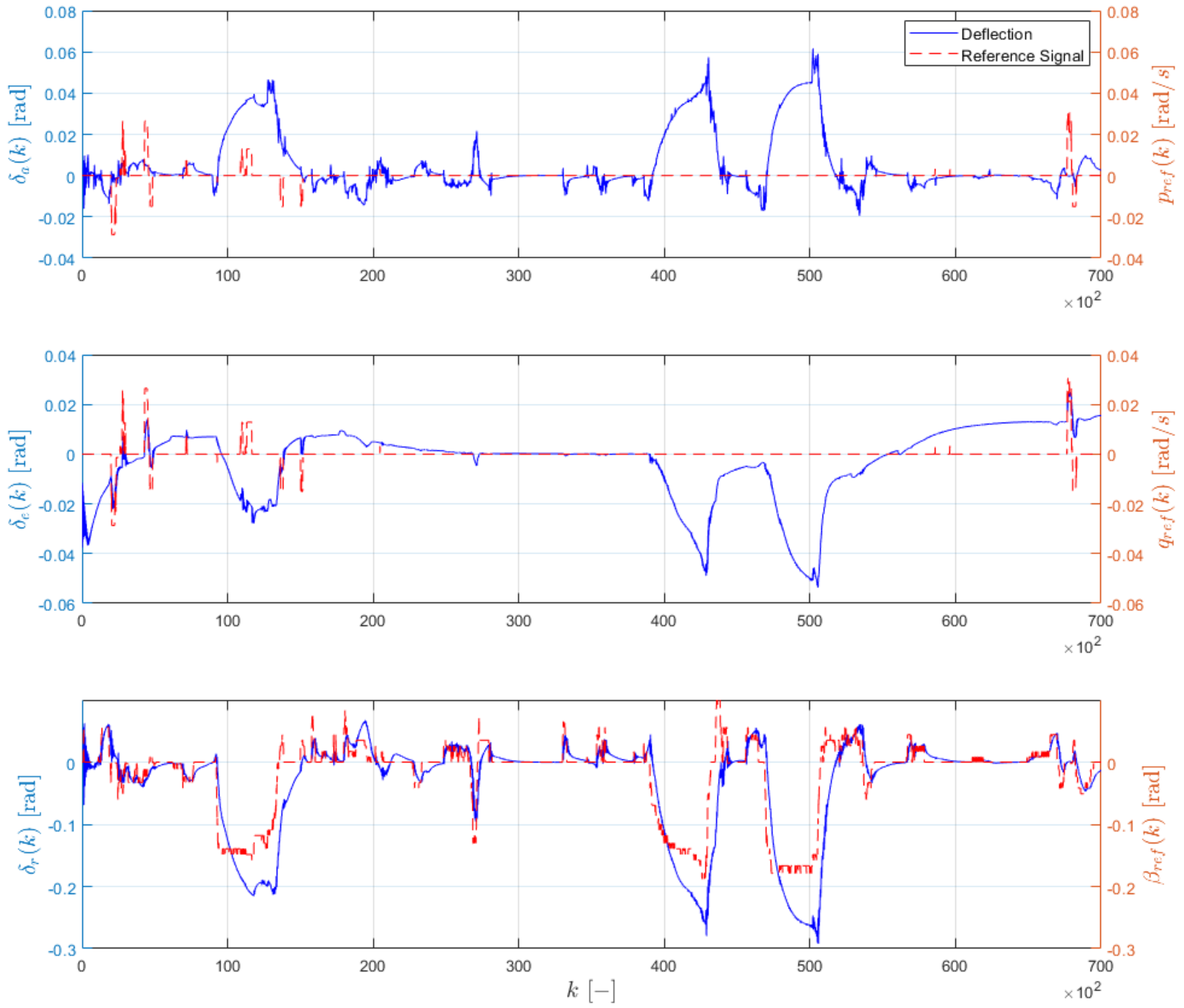

Figure 7.5: Control Surface Deflections & Reference Command Inputs of Validation Flight without Failure using the Manual INDI Controller

7.2.3. Comparison with ANDI & Classical Rate Controller

The INDI controller successfully completed the validation flights with fewer pilot inputs and smoother chnages in the control surface deflections than the other controllers. The INDI controlled aircraft was also more responsive to the pilot's commands than the ANDI controller but less than the classical rate controller. Additionally, the sideslip controller performs best with the INDI controller, virtually no pitch or roll rate inputs are required when performing turns. Overall, the INDI controller performed best in the validation flights however further analysis on other aircraft trajectories and failures as well as subjective analysis from pilots is required before a decisive decision can be taken.

The INDI controller is more resilient to extreme flying conditions than the ANDI controller, the response of the INDI controlled aircraft to pilot inputs in these conditions are generally smoother and more predictable than with the ANDI controller. The INDI controller does not rely on the stability and control derivative estimates from the AMI algorithm significantly reducing the impact of model mismatch in these highly nonlinear situations which the AMI algorithm struggles to accurately model. Furthermore, the INDI controller does not rely on the AMI monitoring algorithm to accurately detect a failure removing a possible point of failure. While the response of the aircraft using the classical rate controller to pilot input's is faster, the response of the INDI controlled aircraft is generally smoother and require less corrections and thus is preferable over that of the classical rate controller.

The INDI controller quickly counteracts the aileron deflection caused by the failure similarly to the other controllers. The main difference between the behaviour of the INDI and ANDI controller is in the effectiveness of the roll rate channel, which is halved for the INDI controller as the control effectiveness matrix in Equation 7.4 does not change after the failure while for the ANDI controller the AMI algorithm detects that the effectiveness of the ailerons are halved as effectively only one aileron is operational in the $C_{l_{\delta_a}}$ estimate, doubling the aileron deflections to compensate. The control derivative estimates of the AMI algorithm could be used in the control effectiveness matrix of the INDI controller to account for the halving of the aileron effectiveness while keeping the impact of model mismatch low.

8
Conclusion

Two nonlinear adaptive flight control approaches, ANDI and INDI, have been analyzed and compared with and without an aileron hardover failure using the provided Cessna Citation simulink model. Both adaptive nonlinear controllers showed promising advantages over the classical rate controller, however the versatility of the classical rate controller is unmatched by the adaptive nonlinear controllers. Further research on failure scenarios and aircraft trajectories is necessary before a decisive decision can be taken on the viability of the analyzed controllers for fault tolerant control.

The ANDI controller relies on knowledge of the system model obtained through online model identification. The behaviour of the ANDI controller is dependant on how accurate the aerodynamic model of the AMI algorithm is at modelling the aerodynamic forces and moments acting on the aircraft. After a failure the AMI algorithm detects changes in the stability and control derivatives of the aircraft, in the case of the aileron hardover failure, the ANDI controller accounts for the halving of the aileron effectiveness by doubling the aileron deflection. In extreme conditions however the aerodynamic model struggles to accurately model the highly nonlinear aerodynamic forces and moments acting on the aircraft resulting in an erratic behaviour of the ANDI controller. The response of the ANDI controlled aircraft to pilot inputs is sluggish compared to the INDI controller, namely due to the limitations of the AMI algorithm.

The INDI controller uses angular acceleration measurements to compute the changes of the control surface deflections. It is more versatile than the ANDI controller as it does not require online model identification thus is not affected by model mismatch. This comes at a cost however, as the control effectiveness matrix of the inner-loop INDI controller does not change after the failure but the aileron effectiveness of the aircraft does, as a result the pilot will feel that the response of the aircraft to the roll rate inputs is halved. Overall, the INDI controller is preferable over the ANDI controller as it is more predictable and has a smoother response to pilot inputs.

Several recommendations are advised that aim to overcome some of the weaknesses of the analyzed adaptive nonlinear controllers. One of which is using other linear regression techniques in the AMI algorithm, such as principle component regression, which is able to increase the accuracy of the parameter estimates in case of multi-collinearity among the predictor variables. It is also recommended to use a more complex aerodynamic model, perhaps one that uses multivariate splines, to further increase the accuracy of the AMI algorithm to improve the behaviour of the ANDI controller. In regards to the INDI controller it is advised to update the control effectiveness matrix with the control derivative estimates of the AMI algorithm to account for the effect of the failure on the control surfaces effectiveness.

Bibliography

[1] J.C. van der Vaart E. de Weerdt C.C. de Visser A.C. in ’t Veld E. Mooij J.A. Mulder, W.H.J.J. van Staveren. Flight dynamics, March 24, 2013.

[2] Parameter estimation techniques and applications in aircraft flight testing, April 24-25 1973.

[3] Eugene A. Morelli. Practical Aspects of the Equation-Error Method for Aircraft Parameter Estimation. *AIAA Atmospheric Flight Mechanics Conference and Exhibit*, August 2006.

[4] A. Vahidi, A. Stefanopoulou, and H. Peng. Recursive least squares with forgetting for online estimation of vehicle mass and road grade: theory and experiments. *Vehicle System Dynamics*, 43(1):31–55, January 2005.

[5] Marco Campi. Performance of RLS Identification Algorithms with Forgetting Factor: A Mixing Approach. page 25.

Appendices

A

Symmetric Control & Stability Derivative Estimates

The time histories showing the convergence of the symmetric stability and control derivative estimates of the validation flights with and without failure are shown in Figure A.1, Figure A.2 and Figure A.3.

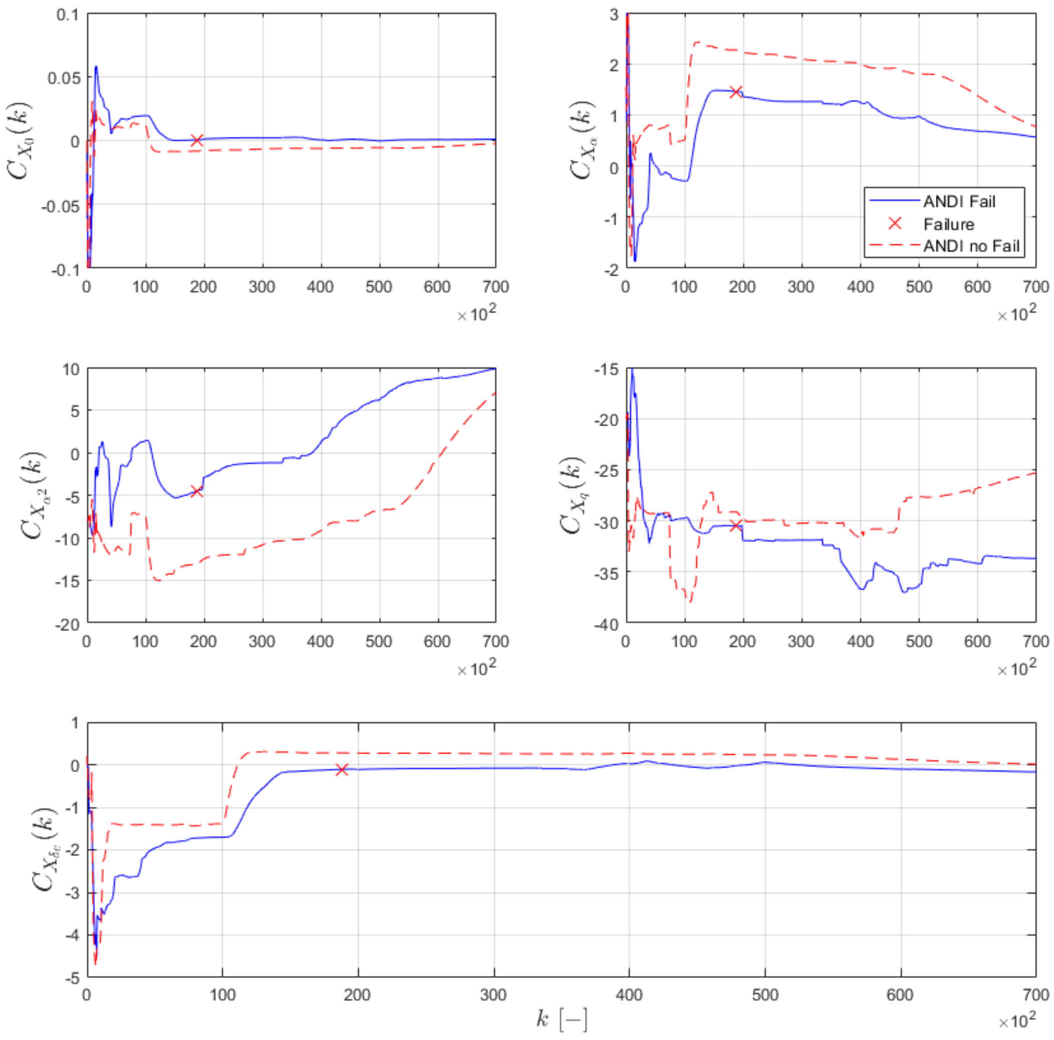

Figure A.1: C_X Stability and Control Derivative Estimates of Validation Flights using the Manual ANDI Controller

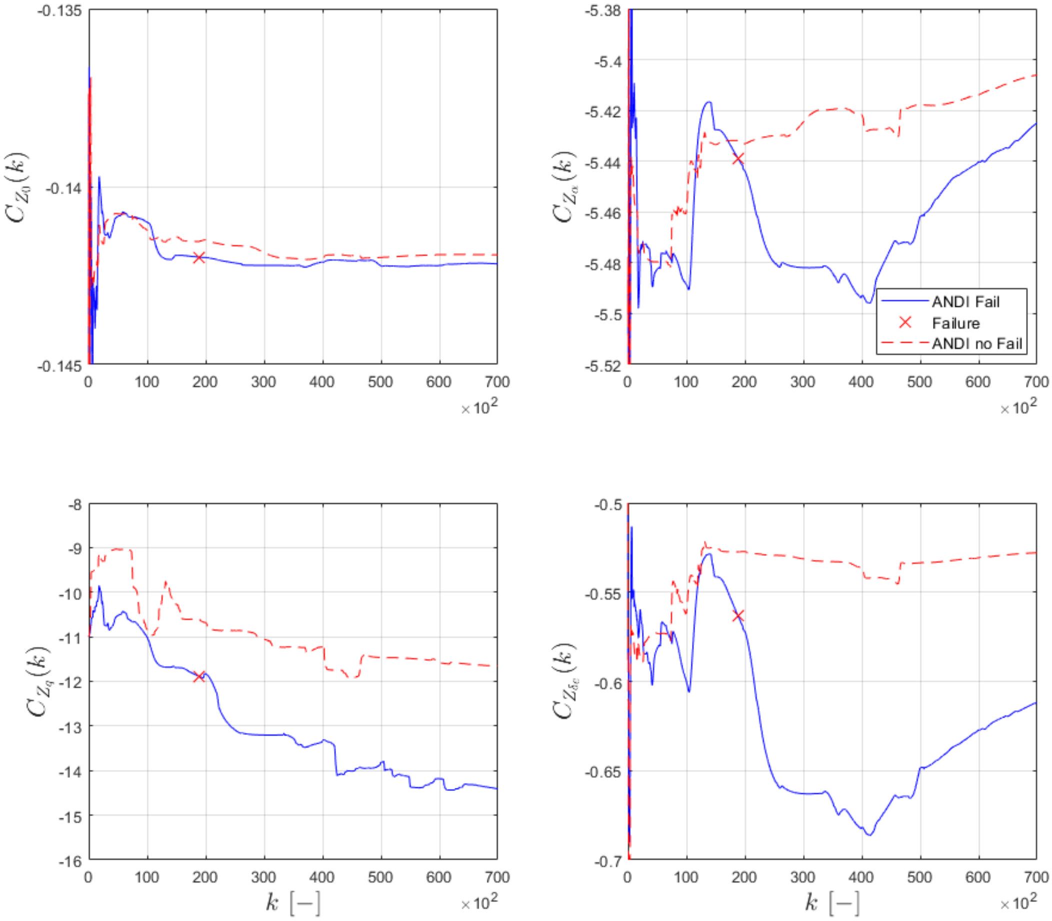

Figure A.2: C_Z Stability and Control Derivative Estimates of Validation Flights using the Manual ANDI Controller

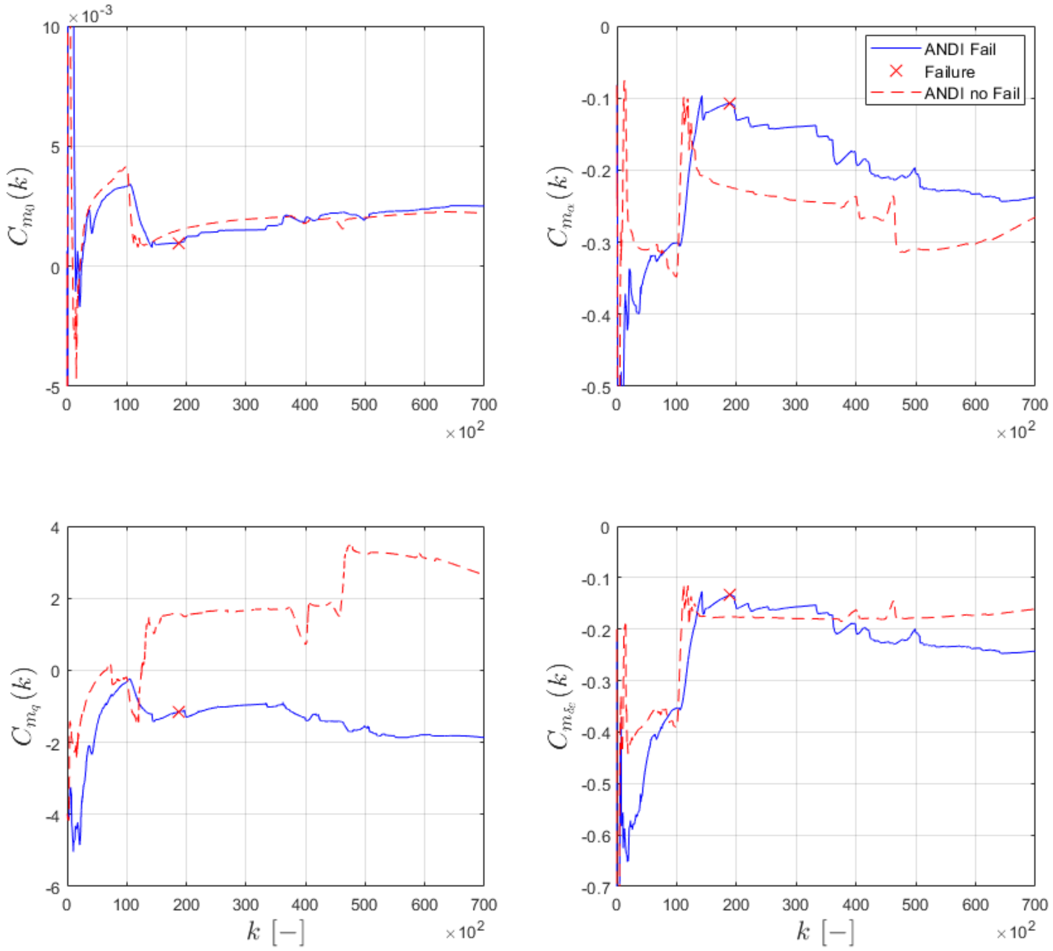

Figure A.3: C_m Stability and Control Derivative Estimates of Validation Flights using the Manual ANDI Controller